ANALYSIS ON SEPARATED REGIONS IN INTERNAL FLOWS THROUGH PARTICLE IMAGE VELOCIMETRY

by

John C. Paulson

A Thesis

Submitted to the Faculty of Purdue University

In Partial Fulfillment of the Requirements for the degree of

Master of Science in Mechanical Engineering

School of Mechanical Engineering

West Lafayette, Indiana

May 2022

THE PURDUE UNIVERSITY GRADUATE SCHOOL
STATEMENT OF COMMITTEE APPROVAL

Dr. Guillermo Paniagua, Chair
School of Mechanical Engineering

Dr. Terrence R. Meyer
School of Mechanical Engineering

Dr. Matthew J. Bloxham
School of Mechanical Engineering

Approved by:
Dr. Nicole Key

Dedicated to Dr. Paul Mlakar. His belief in me as a young cadet West Point and his mentorship throughout my ten years in the army led me to be where I am today.

ACKNOWLEDGMENTS

The author would like to thank Dr. Guillermo Paniagua and the PETAL team and members of the Tebbe TDI Laser Lab for their support and assistance with this work. The author would like to also acknowledge the Rolls-Royce Corporation for their technical and financial support.

TABLE OF CONTENTS

LIST OF TABLES

LIST OF FIGURES

LIST OF ABBREVIATIONS

BFL:	Back Focal Length
CFD:	Computational Fluid Dynamics
CMOS:	Complementary metal-oxide semiconductor
DSR:	Dynamic Spatial Range
DVR:	Dynamic Velocity Range
FOV:	Field of View
LEAF:	Linear Experimental Aerothermal Facility
LES:	Large Eddy Simulation
LPT:	Low-Pressure Turbine
Nd:YAG:	Neodymium-doped Yttrium Aluminum Garnet
PETAL:	Purdue Experimental Turbine Aerothermal Laboratory
PIV:	Particle Image Velocimetry
RANS:	Reynolds-averaged Navier-Stokes
TR-PIV:	Time Resolved-Particle Image Velocimetry
URANS:	Unsteady Reynolds-averaged Navier-Stokes

LIST OF SYMBOLS

c_{max}:	Pixels travelled by particle in image window for "1/4 rule"
c_r:	Pixels (samples) per image diameter of particle
c_τ:	Constant – ability to determine displacement
d_B:	Beam diameter
d_r:	Camera pixel size
d_p:	Particle diameter
h:	Laser light sheet height
L_x:	Image length
u_{max}:	Freestream velocity
$\Delta x_{p,max}$:	Particle distance in freestream velocity
t:	Time
δ_z:	Depth of view
Δ:	Change
λ:	Light wavelength

ABSTRACT

For internal flows, the detachment of the boundary layer is a major contributor to pressure loss. To improve efficiency, it is essential to characterize these regions to understand the location and magnitude. Particle Image Velocimetry (PIV) is applied to provide time-resolved measurements to achieve accurate results without perturbing the flow. This thesis covers the methodology for creating an adaptable optical measurement technique in a high frequency study of separated regions in transonic internal flows. Focus on the optimization of the laser optical array and image acquisition system yield improved Dynamic Spatial Range (DSR) and Dynamic Velocity Range (DVR). Further analysis is provided on the flow dynamics of the seed particle, with local seeding solutions provided for improved seeding density in high-speed flows for various geometries. Light scattering efficiency of the particle is also analyzed to completely define the desired particle size. Two pulse-burst Nd:YAG lasers and two high speed cameras are used in this study to achieve a frame straddling technique necessary to resolve high frequency flows. Comparison of the recording media to the DSR highlights performance costs and benefits between the two cameras. Uncertainty measurements are determined from the calculated setup and compared to correlation statistics-based uncertainty quantifications. Image processing and cross-correlation software are used to provide analysis on the flow characteristics for two separate studies with comparison to Computational Fluid Dynamic predictions.

1 INTRODUCTION

Near wall flows, seen in finned heat exchangers and turbine airfoils, experience an adverse pressure gradient which results in the separation of the boundary layer from the surface. In this separated region, recirculation occurs due to the reversal of flow. In a finned heat exchanger, this separation region negatively impacts the design's ability to effectively extract heat from the system. For turbine airfoils, specifically in a low-pressure turbine used at high altitudes, the turbine's performance diminishes as the flow separation reduces the power it can extract.

When designing such geometries, CFD is a common tool utilized to predict these flow interactions. Furthermore, CFD is used to optimize a design through geometrical changes or active flow control parameters. Pressure, temperature, and velocity can be obtained using point-wise measurement probes to confirm the CFD results. These measurements, however, are limited in their spatial resolution and may cause flow perturbations with any object introduced into the flow path. Particle Image Velocimetry is non-intrusive optical measurement technique which can provide information on a velocity field at a separated region. The added benefit to PIV is the ability to instantaneously measure a large region of interest without the added requirement of area traverses when compared to point-wise measurement techniques. Challenges still exist in achieving accurate and spatially resolved measurements in a separated region for PIV and require an adaptive solution for various test articles and conditions.

When developing a PIV measurement system, special considerations must be considered on the particle dynamics and light scattering characteristics to produce accurate flow tracking from the seed. Understanding the capabilities and limitations of a particle's size and density will allow the user to determine the velocity lag and signal-to-noise ratio of the particle in the measurement system. This determines the accuracy of the information from the PIV system. The quality of the flow field information is given by the range of velocities that can be resolved, and the overall resolution the flow field provides. Several factors are discussed in this work regarding these ranges and how recent techniques can assist in providing improved velocity and spatial ranges, as well as defining these characteristics in detail.

1.1 Literature Review and Particle Image Velocimetry

Particle Image Velocimetry measures the particle displacement of the seeded flow over a short time span with the use of a laser and high-speed camera. The particle must have physical characteristics close to those of the fluid they are seeded in to remain accurate to the flow. As the particles travel with the flow, a laser is used with spherical and cylindrical lenses to create a thin light sheet to illuminate the particles in a specific region of interest. The laser light diffracts off the particles at a desired repetition rate and a short exposure time and are visible in a high-speed camera during each laser pulse. The high-speed camera, synchronized with the laser, captures the images of the particles at a specific location in time. The time between images is known based on the sampling rate of the camera. Given this change in time and the distance traveled for the particles between two images, the resulting vector field is determined using a cross-correlation technique.

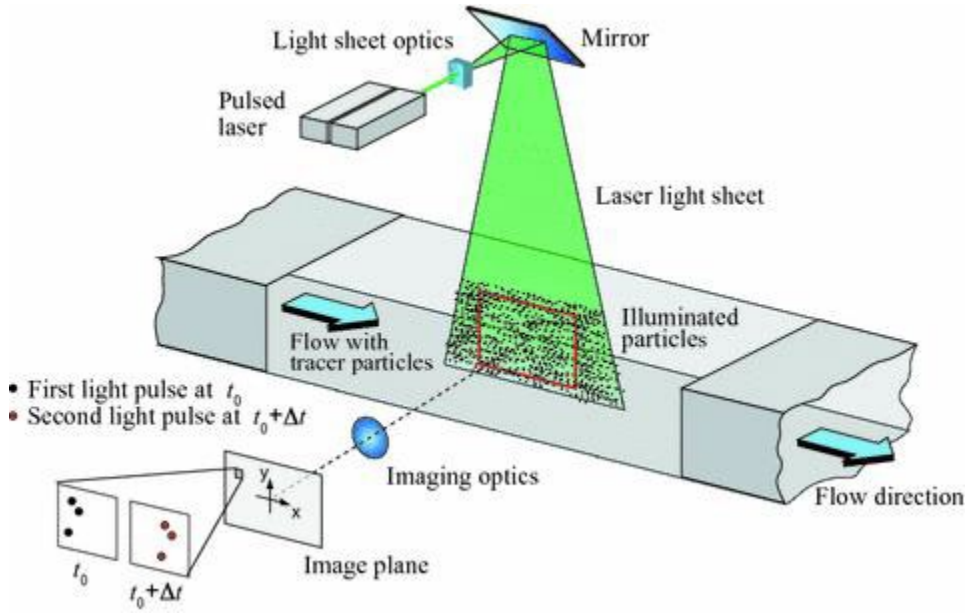

Figure 1.1 Depiction of a 2D Planar-PIV Setup [1]

As achieving a near matching density of the particle to that of air is difficult, the particles are reduced in size on the order of microns to avoid gravitational affects influencing the suspended particles [1]. Duzgun provided an in-depth analysis of particle dynamics and various seeding options for use in internal flows [2]. Employing a tracer particle that best matches the fluid's characteristics in PIV is essential to accurately measure the fluid flow in turbulent

regions. Density, dynamic viscosity, and particle diameter are critical properties when choosing the most applicable particle. For measuring airflow at a high Reynolds number, common particles include polystyrene, air bubbles, and oils. Duzgun's research on alginate particle characterization proved this material's improved performance in faithfully following the fluid flow when compared to commonly used tracer particles. After creating a process to reduce the alginate particle diameter to 0.2μm, Duzgun yielded an ideal particle size with a porous membrane structure as seen in the figure below.

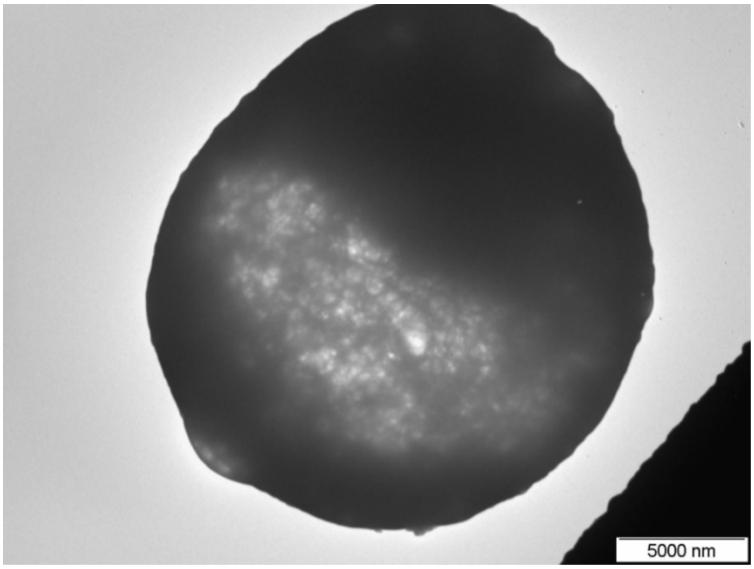

Figure 1.2 Alginate Particle with Porous Membrane [2]

The significance of the porous membrane is the material's ability to assume the density of the surrounding fluid. This structure reduces the velocity lag seen in the more commonly used tracer particles and gives the alginate particle a soft texture which reduces risk to any instrumentation in the test region. The size, density, and shape of the particle as well as the enclosed geometry the flow travels through determines the time response of the particle, or its ability to faithfully follow the flow.

While a smaller particle proves beneficial to accurately measure a flow field, there are negative impacts that affect the overall measurement system. Light scattering capabilities of the particle are considered to ensure a high signal-to-noise ratio when capturing images of the particles in the laser light sheet. As a particle's diameter is related to its ability to scatter light, a smaller particle will appear dimmer in the laser pulse. Increasing the power of the laser is not a

feasible option as this is dependent on the output of the laser, and more importantly, may result in unwanted reflections from the surroundings which introduce noise to the captured image. Duzgun addressed this characteristic and mitigates the reduced light scattering of the smaller alginate particle by applying a fluorescent dye [2].

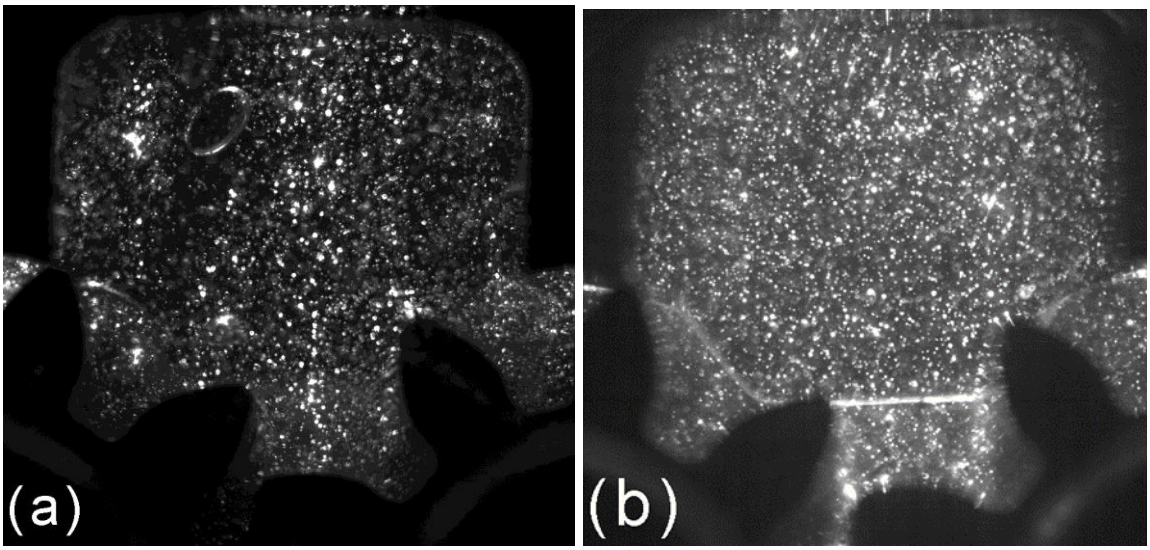

Figure 1.3 Comparison of Air Bubbles (a) and Dyed Alginate Particles (b)

When reduced to a smaller particle size of 0.2μm, the alginate particle suffers in its light scattering ability. Duzgun corrected this shortfall with a florescent coating which achieved desired results. The figure above shows a comparison of air bubbles (a) and the alginate particle with the florescent dye (b) flowing through an external gear pump using a 532nm ND:YAG green laser. The alginate displays a more uniform dispersion throughout the interrogation region and a strong light scattering capability with the addition of the florescent dye. Duzgun goes on to compare the time step and displacement error for the above particles which shows the alginate particle significantly outperforming the air bubbles. While the porous membrane of the alginate particle performed well for Duzgun, the main drawback to this seed material is the maintenance required between measurements. Duzgun noted that the alginate particles collected and smeared the window access points to the test section and severely reduced the quality of the images. Routine disassembly and cleaning were required after a few iterations before further testing was possible.

While oil based seed particles may also smear across the test section windows, the risk is reduced compared to a solid seed particle as the former is less opaque. Molezzi developed a PIV measurement system for high-speed separated flows focusing on improved spatial resolution and accuracy of the PIV technique [3]. The difficulty in measuring separated regions is the particle's ability to follow the flow through high gradients. Vortices in the separated region will carry particles out of the region and reduce the seeding density of the measured area. Molezzi employed a TSI silicone oil atomizer through a semi-local port upstream of the test section. A rake system is used matching the full span of the test section in a single plane matching the location of the downstream light sheet. The seed is introduced into the settling chamber upstream of the final honeycomb to ensure uniform dispersion and full mixture in the flow. Tests are done at low and high-speed flows to conduct baseline assessments of the seed density in the captured images. Molezzi's focus on spatial resolution show the relation between the seed density and the allowable interrogation window size used in the cross-correlation method. As the interrogation window yields an averaged velocity component for that spot size, the particles present must be small enough to fit in the window and have a large enough distinguishable displacement between the image pair. The most important factor stated is the uniform density of imaged particles throughout the entire region of interest to allow for thoroughly interrogated image pairs. A lighter density, typically in the separated region, will limit the smallest interrogation window allowable and reduce the spatial resolution for the overall image.

Major developments in PIV come from the improvement of the high frequency capabilities of the laser and camera. In the past twenty years, these two technologies have improved to resolve flow features in the kHz range [4]. Time-resolved PIV in the transonic and supersonic regions are now achievable. Recently with the introduction of ultra-high-speed cameras and pulse-burst lasers, sampling frequencies are achieved in the magnitudes of MHz. The pulse-burst laser differs from the traditional single head laser with the ability to create pulse pairs, or doublets, with a varying delay time from the first pulse to the second. This technology introduced the ability to capture high frequency flow phenomena at a moderate sampling rate. Beresh explained how the development of time-resolved PIV allows the user to create a time-series of instantaneous velocity fields to extract high frequency phenomena in the instantaneous flow field and low frequency flow structures over the entirety of the sample time [4].

In 2015, Beresh conducted a 2C PIV measurement in Sandia's Trisonic Wind Tunnel for TR-PIV for turbulent eddies [5]. He noted that placing two large Photron SA-X2 cameras next to each other enabled a larger combined FOV but at the sacrifice of a 2% error due to the camera angles canted at 5 degrees to create a seamless FOV from one camera to the next. Beresh explained that while a pulse-burst laser is limited for its low duty cycle and 10.2ms duration, this is a long enough measurement time for most high frequency phenomena. The figure below shows the various eddies that form at M3.7 for time increments in the magnitude of 40μs. These structures are observed for their full period at 25 kHz using a pulse-burst laser. Beresh applied this technique to cavity flows and measures the velocity power spectra to measure the acoustic tones present in the flow. He further explains that through TR-PIV, these acoustic resonances can be mapped and can provide insight to their origins.

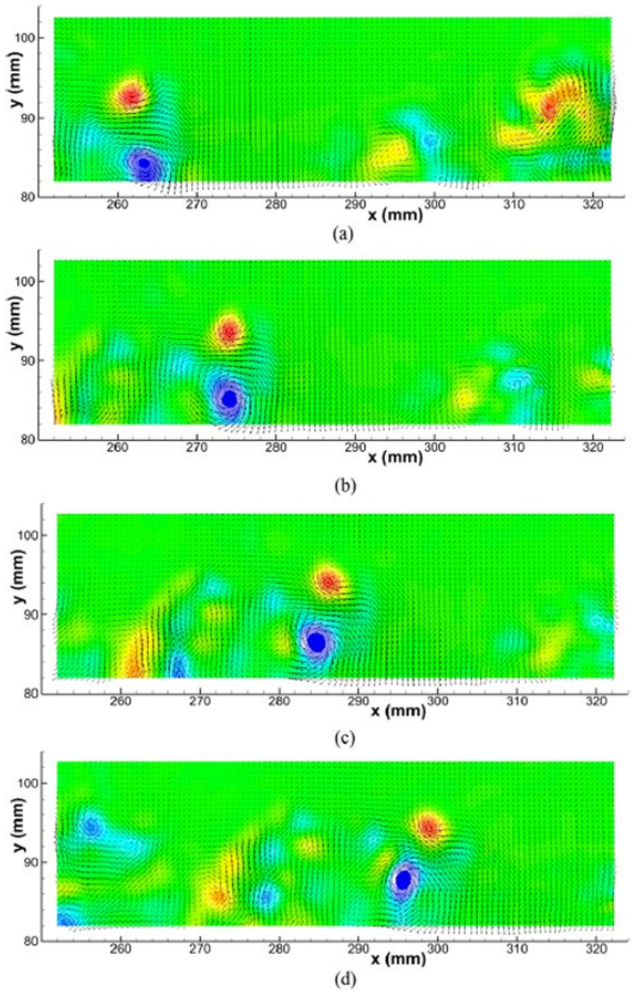

Figure 1.4 Instantaneous Velocity Fields at 40μs Intervals Extracted from a 2.5ms Sample from a Pulse-Burst Laser at 25kHz [5]

The experiments use a QuasiModo-1000 pulse-burst laser at 50 kHz with the Photron cameras at 50 kfps to sample turbulent structures at 25 kHz. Higher frequencies can be achieved; however, this would sacrifice the resolution and field of view. An issue during his experiment rooted from the 20μm pixel size of the Photron camera. This is three times larger than typical PIV cameras and come with a greater risk of peak locking if the particle size is measured only in one pixel. The camera optics are adjusted to ensure an imaged diffracted particle size larger than one pixel to avoid peaking locking. Beresh explained that the pixel density of the camera sensor limits the spatial resolution available and results in sparser vectors in the resolved flow field.

The number of vectors resolved in a region of interest and the smallest resolvable velocity are determined by the dynamic spatial range and dynamic velocity range. Adrian explained that the optimization of the camera's optics can maximize the information obtained from a resolved flow field [6]. The dynamic velocity range is the ratio of the maximum resolvable velocity to the minimum based on a fixed set of operating settings. The dynamic spatial range is the ratio of the object's field of view to the smallest resolvable spatial change. In other words, it is the ratio of the number of vectors in a linear field of view. This characteristic of the PIV measurement system is significant to turbulent regions to measure small scale velocity gradients in a larger flow field. Adrian goes on to explain the relation of the camera attributes, the time delay between images, and the imaged diffracted particle. The relations are derived to equations optimizing the magnification and f-number of the camera to yield a high DVR and DSR. Adrian applied these equations to various recording media given their sensor size and pixel size to set upper bounds to the spatial and velocity ranges. While the velocity range can be fixed for many cameras as the variables are independent of the recording medium, the spatial ranges determined by pixel size and sensor length can range from an order of 10 to 10,000. A final look at the developed system then yields the resulting measurement error. Further discussion on these equations and their application are provided in chapter 2.

Hain expanded on Adrian's findings with the development of high-speed CMOS cameras. While the sampling rate of these cameras increase the range of applications to flow measurements, the CMOS sensors are typically smaller than their CCD counterparts in both area and pixel size. This compromise naturally reduces the spatial range achievable down to 30 [7]. Hain suggested several options to improve the DSR and DVR for a PIV system during the cross-correlation method. Multiframe PIV is discussed to increase the velocity range. In this technique,

one image is correlated to several subsequent images to assist in resolving smaller particle displacements.

Persoons developed a multiple pulse separation technique to further improve the DVR of a PIV measurement. In this method, recorded images are subjected to varied laser pulse separations. This enhanced laser capability allows for resolution of particle displacements in high and low speed flows throughout the region of interest. Persoons also discussed the multi-pass correlation technique common in modern cross-correlation software. The initially large interrogation window for the first pass follows the "1/4 Rule" imposed by Adrian. While the larger particle displacements are determined, smaller displacements cannot be resolved. Subsequent passes employ a smaller window along with the displacement information found from the previous pass. This window reduction allows for an improvement in the smallest resolvable displacement. A second impact of this method is the smaller averaged spot size. The smaller interrogation windows in the following passes allows for more independent vectors resolved in the field of view for a larger spatial range.

1.2 Definition of the Research Objective

This thesis provides a study on the separated regions in a finned heat exchanger and a low-pressure turbine airfoil. Several challenges are faced when applying PIV at the boundary layer. First, the particle dynamics must be understood to ensure the particles not only track the flow but are also present in the separated regions. Particles will typically concentrate at the shear layer but are unable to enter the boundary layer [1]. While the boundary layer can be identified in this instance, any recirculation or frequency analysis on vortex shedding is unavailable.

As flow separation occurs, a strong gradient is present between the freestream velocity and the recirculation region. The camera's optical set up is optimized to resolve these changes in velocity. As a higher dynamic velocity range and dynamic spatial range result in more information from the flow field, it is critical to determine the best setup for the image acquisition system. For analysis at a separated region, a high DVR will ensure minimal data is lost at the region of interest. While modern cross-correlation software can improve the spatial range of the flow field, an initial look at the DSR is needed to obtain the most information at the separated region to fully capture the high gradient of the shear layer, and any turbulent structures inside the separation bubble.

The optical set up and particle characteristics provide quantification of the measurement uncertainty. As the imaged particles are the spot diffractions of the particles when illuminated by the light sheet, there is an unknown error associated with the real particle's true location [6]. This uncertainty is determined by the optical and particle parameters and can be compared to the statistics-based uncertainty quantifications from commercial PIV software. Determining this measurement system uncertainty during setup of the technique can address shortfalls in the optical design prior to testing and improve measurement accuracy.

With the objective to **create a PIV measurement system adaptable to various geometries in transonic flows**, the author sets out to develop an adjustable seeding technique that balances the demand for the particle to accurately track the flow and provide a strong signal-to-noise ratio through its light scattering capabilities. Additionally, an image acquisition tool to ensure high DVR and DSR is developed. Finally, the two methods above are utilized to yield a low measurement uncertainty and results in a reduced uncertainty for the resulting vector field.

1.3 Research Methodology

The **development of an adaptable seeding technique** requires the characterization of the particle. For two different studies, the time response of the particles is assessed to ensure accurate depiction of the flow. For the given Smoke-180 oil used to create the seeding particles and the characteristic length of the two geometries measured, the Stokes number of the particle is determined. This relationship in time response of the particle to the fluid flow is dependent on particle size and defines how well the particle will track the flow accurately. To ensure that the particles are present in the separated regions, a priming technique is applied from a global seeding port. A final characteristic of the particle is assessed based on Mie's scattering theory.

With the ideal particle size determined, the **optics optimization tool** is employed to achieve high spatial and velocity ranges. The optical setup for the image acquisition system is calculated based on the region of interest, flow conditions, and parameters for the particle and camera. By defining the optical setup to yield a high DVR and DSR, the setup is refined without compromising the time response or light scattering efficiency of the particles. The optimization determines the magnification and f-number of the camera lens used to adapt to the above parameters. The result is a user friendly tool formatted in excel to rapidly explore different optics

and particle settings to determine the best setup. This tool allows for repeatability of experiments, or updates to an optical setup if as the test campaign develops.

Calculations are done to determine **measurement system uncertainty** based on the refined optical setup and particle size. This uncertainty is based on the true location of the real particle versus the known location of the imaged particle. With an optimized system, the unknown error is reduced and are related to the reduced uncertainty quantifications for the resulting flow field.

The resulting setup is then built around a linear wind tunnel with top and side optical access windows for the laser and camera. The system is aligned, and the laser and camera are synchronized for the desired sampling rate. Initial results compare different seeding techniques to achieve sufficient particle presence in the separated regions. Further analysis is done to confirm the particle characteristics match those determined in the previous research objectives.

1.4 Thesis Layout

This thesis covers the development of the measurement technique in chapter 2 with a facility review on the linear wind tunnel and the test articles studied. The seeding system is explained with an analysis of the particle time response compared to the two experiments conducted. Next, the optical setup and optimization is discussed, and the measurement errors are determined. Chapter 3 introduces the experimental setup and procedures, and the resulting particle images and flow fields are analyzed. The spatial and velocity ranges of the processed images of the separated regions are assessed and the resulting velocity fields are compared to CFD. The measurement system uncertainties are compared to the uncertainty quantifications determined through LaVision's DaVis 8 software. Chapter 4 discusses the success of the strategy employed to achieve the objective of an adaptable PIV measurement system in transonic flows. Future work is provided on the continued development of the adaptable seeding system for local seeding and sonic flows.

2 DEVELOPMENT OF THE MEASUREMENT TECHNIQUE

2.1 Description of Linear Wind Tunnel and Test Articles

The facility used in this study at Purdue Experimental Turbine Aerothermal Laboratory (PETAL) is the Linear Experimental Aerothermal Facility (LEAF). Figure 2.1 depicts the full layout of the facility from the air storage tanks with a capacity of 138 bar to the linear wind tunnel located top middle, and finally to the exhaust air tanks which can be used under vacuum or ambient conditions. The air supplied by the storage tanks are controlled by mass flow directly from the tanks, or through a heat exchanger with a maximum temperature of 800 K. The combined hot and cold supplies can provide a maximum mass flow of 27 kg/s. From the mixer, the air passes through a critical venturi allowing for an accurate mass flow before entering the settling chamber. Upon actuation of the nitrogen controlled fast opening valve, the air enters the settling chamber to ensure uniformity in the flow. The settling chamber's divergent-convergent structure slows the flow to prevent upstream flow disturbances. The flow is then accelerated into the linear test section.

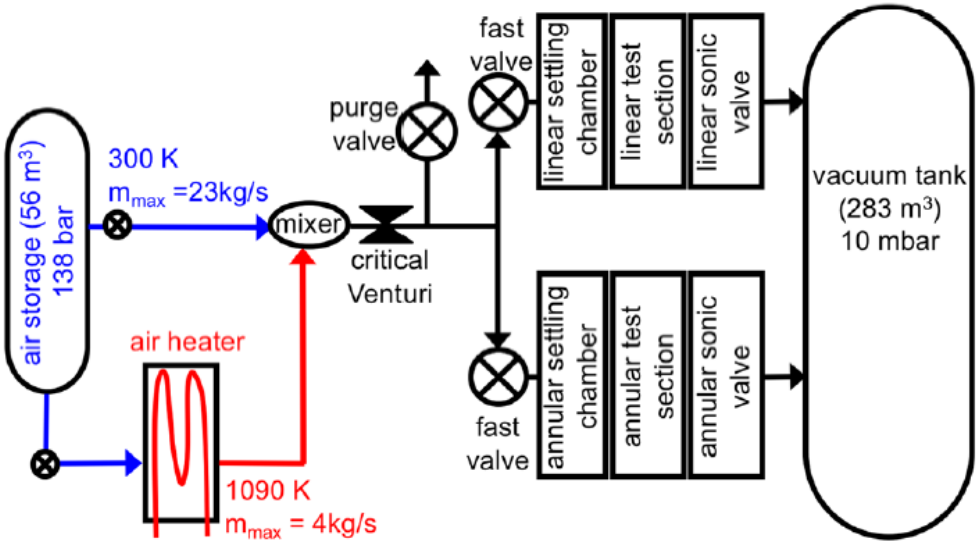

Figure 2.1 Schematic layout of the PETAL Facility

Figure 2.2 depicts the settling chamber and linear wind tunnel with airflow traveling from left to right. Note that the flow is dispersed radially when entering the settling chamber to ensure uniformity. The honeycombs along with the inner conical structures reduce any turbulence as the

flow enters the test section. An optimized transition passage was designed to account for the change in geometry as the flow enters the rectangular test section.

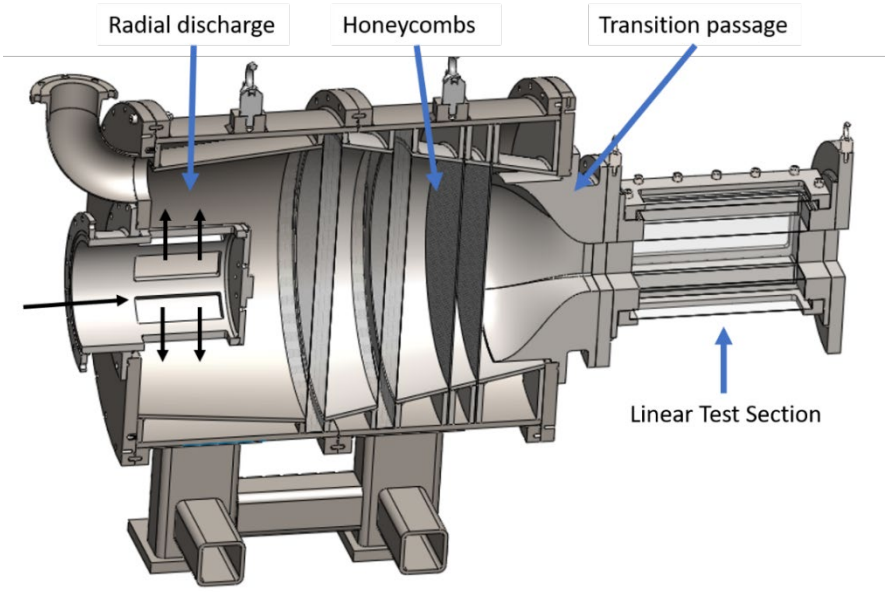

Figure 2.2 Settling chamber and test section of the linear facility

LEAF is a modular test section designed to incorporate various internal flow geometries while allowing for several point-based and optical measurement techniques. All four walls are removeable and can be configured for windows, or various wall inserts. Steel frames fixed to the test section with 14 bolts are used to ensure a tight fit of the walls to the test section, preventing any loss of pressure through the test section. Figure 2.3 shows the LEAF configuration used in both the finned heat exchanger and low-pressure turbine experiments. From the top, a tri-insert wall is used to insert probes to measure the pressure and temperature. The middle insert, in blue, represents the quartz window to allow the laser sheet access into the test section. The side view displays the test section with the finned heat exchanger from a profile view with a full-sized quartz window between the viewer and the test article. This window allowed for full optical access for the image acquisition system.

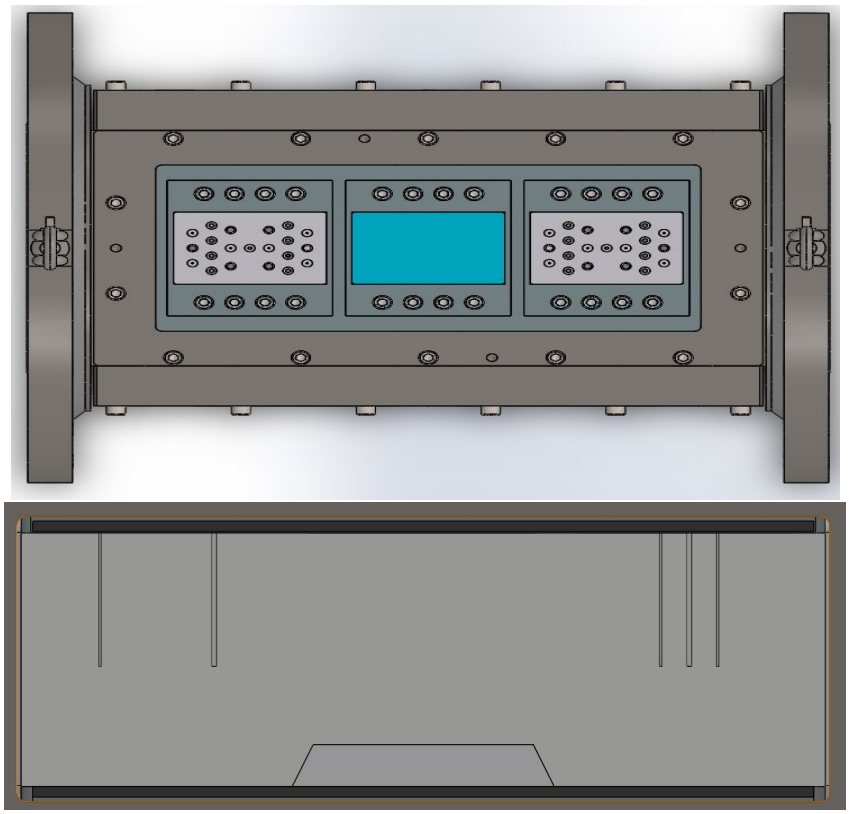

Figure 2.3 Top and Side Views of LEAF with Optical Access

The two geometries studied in this work are depicted below in Figures 2.4 and 2.5. First, the finned heat exchanger is examined. From hub to tip, the fins have a length of 175mm to 147mm and a height of 28mm. Each fin has a thickness of 1.4mm and a spacing of 3mm between each fin. The fin thickness of 1.4mm will be referenced later for the characteristic length in determining the time response of the particles. The heat exchanger is made of aluminium 6082 T651 and is mounted into the test section from the base wall. From the top view of the heat exchanger, a total of 97 pressure taps are seen. The optimized finned heat exchanger seen in the bottom of figure 2.4 is the result of numerical analysis performed at the Universidad Politéncia de Madrid [9].

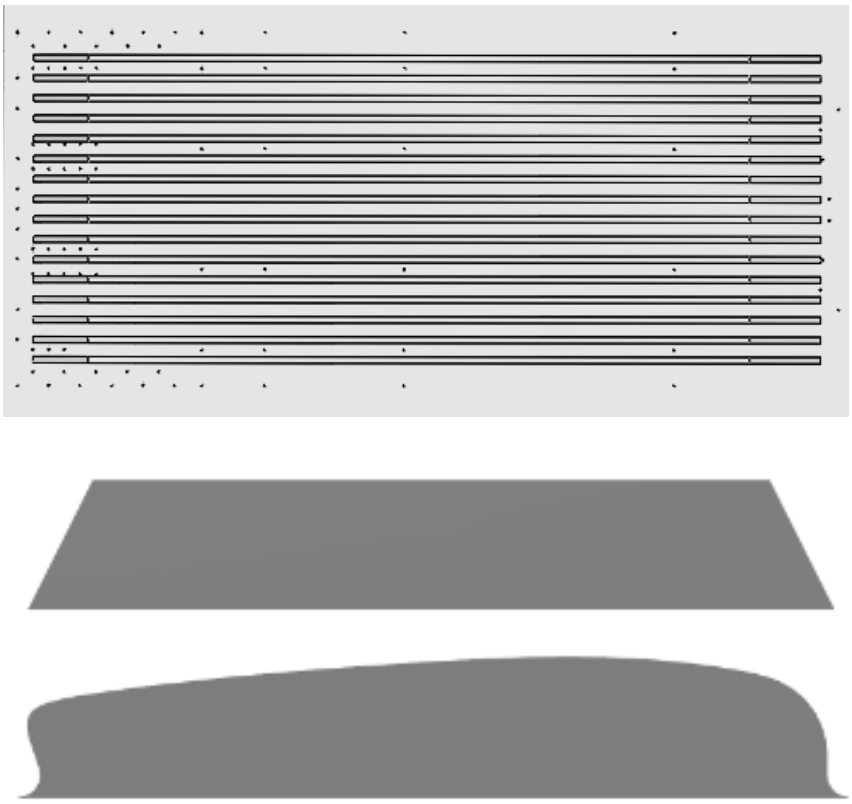

Figure 2.4 Top and Side View of the Baseline and Optimized Finned Heat Exchanger

The LPT wall-mounted hump evaluates flow separation in a low-Reynolds regime for transonic flow conditions. This design incorporates active flow control through 15 injection ports just past the crest of the hump. Capable of pulsating flow at a range of frequencies, this flow control is designed to reduce the separated region and improve the performance of the LPT [10]. The hump has a characteristic length of 37.51mm which will be used later to determine the Stokes number for the particle.

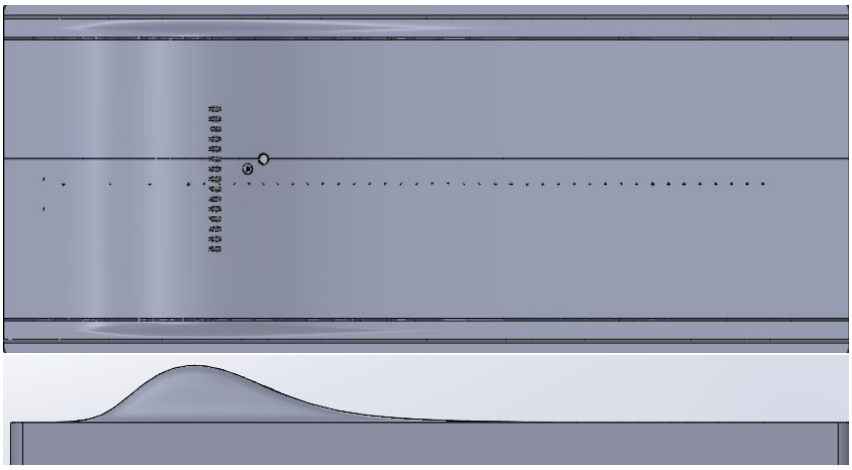

Figure 2.5 Top and Side Views of the Low-Pressure Turbine Hump

2.2 Characterization of the Seed Particle

A custom built ViCount Smoke generator was used to introduce particles into the test section through a global seeding port in the settling chamber. The particle is produced by heating Smoke Oil-180, a mineral oil, and mixed with pressurized nitrogen to create a particle diameter, d_p, of approximately 1μm. The Smoke Oil-180 is used for its lower density and adjustable particle size in the seeder. An added advantage of the oil is its more transparent quality when compared to solid seed materials. As particles begin to accumulate on the windows of the test section, solid particles pose a greater risk of smearing or blocking the view of the camera. An internal regulator allows for the adjustment of the oil-to-nitrogen mixture to yield a thicker smoke with larger particles. The regulator can reduce the ratio as well; decreasing particle size to approximately 0.3μm. Observed later, this control allows for a balance between the particle's accurate tracking in the flow and its light scattering capabilities.

To understand the particle's ability to track the flow, the Stokes number is determined for this seeding material given the equations below. The Stokes number equation is derived from Stoke's drag law which is used to determine the velocity lag between the particle and the true flow. Based on the larger density of the oil particle when compared to air, a smaller diameter particle is preferred to reduce this velocity lag. The time response of the particle, τ_p, is determined on particle size, particle density, and dynamic viscosity of the fluid. The fluid time response, τ_f, is dependent on the maximum velocity expected and the characteristic length of the test article. This characteristic length for the two studied refer to the fin thickness for the finned

heat exchangers, and the height of the hump for the low-pressure turbine wall-mounted hump. The ratio between the particle and fluid time responses is the Stokes number. A low value less than 1 ensures that the particle will generally follow the streamlines of the flow, whereas a value less than 0.1 dictates that the particle tracing error reduces to 1%.

$$St = \frac{\tau_p}{\tau_f} \qquad (1)$$

$$\tau_p = \frac{\rho_p d_p^2}{18\mu_f} \qquad (2)$$

$$\tau_f = \frac{l_c}{U_{max}} \qquad (3)$$

The table below compiles the physical characteristics known for Smoke-Oil 180 and the expected flow conditions for the finned heat exchangers and the wall-mount hump. A particle diameter of 0.3μm and 1μm are calculated to compare the particle's performance in the flow for each case.

Table 2.1 Particle Performance for Various Testing Parameters

Fluid Variables		Finned Heat Exchanger		LPT Hump	
$\mu_f\ [\frac{kg}{m*s}]$	$\rho_p\ [\frac{kg}{m^3}]$	$l_c\ [m]$	$U_{max}\ [\frac{m}{s}]$	$l_c\ [m]$	$U_{max}\ [\frac{m}{s}]$
$1.81 * 10^{-5}$	830	0.0014	150	0.03751	284
Stokes at 0.3μm		0.024		0.002	
Stokes at 1μm		0.27		0.02	

The Stokes number at 0.3μm is given as this size is easily obtained by fully opening the seeder's regulator as stated by the manufacturer. From the Stokes number, it is seen that the particle will find equilibrium in the flow very quickly and perform well to any transient response. Increasing the particle size to 1μm still shows good response to the flow for both test articles, but only the LPT Hump being below the 1% error threshold. The magnitude of the difference between the two cases is due to the characteristic length. The particle will have a greater velocity

lag when the flow interacts with the leading edge of the fins when compared to the larger contour of the hump.

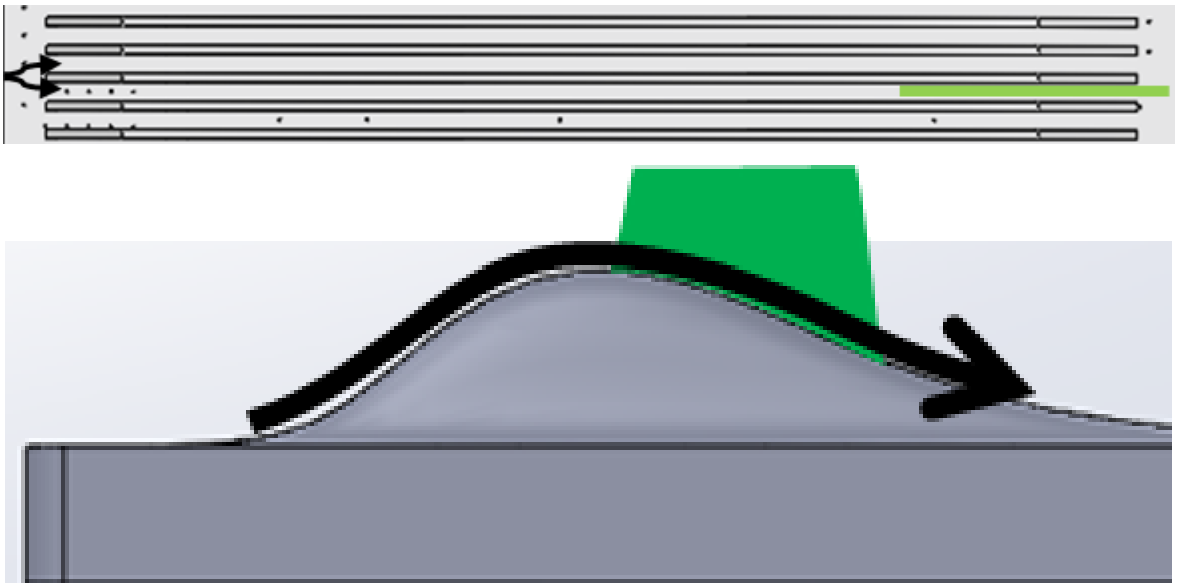

Figure 2.6 Particle Direction of Travel along the Characteristic Length

While Table 2.1 argues that the particle size of 0.3μm is the better size, another critical particle characteristic is considered. The light scattered by the particle is dependent on the particle size. Mie's scattering theory explains the relation between the particle's size to the wavelength, λ, of the incident light [1]. The light scattered by an oil particle of spherical shape has a polar distribution with its highest intensity paraxial to the incident light as seen in figure 2.8. Typical planar PIV, single camera, experiments orient on the image orthogonal to the light sheet due to depth of field and calibration of the images, but it is significant to note the light intensity changes for a particle when viewing from an oblique angle.

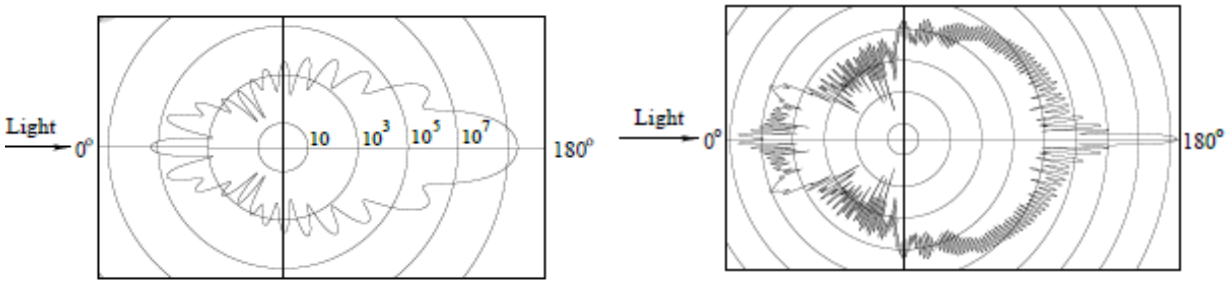

Figure 2.7 Light Scattering Intensity for an Oil Particle of Diameter 1μm (left) and 10μm (right) in Air [1]

The comparison of light intensity in figure 2.7 highlights the significance the particle diameter plays as both figures share the same light intensity logarithmic scale. From the previous Stokes number calculations, it is inferred that a particle size of 10μm would perform poorly in both test cases. With the introduction of the figures above, however, it is determined that a particle size of 0.3μm will perform well in the flow but have poor light scattering efficiency. In early calibrations with the seeder, the regulator is reduced to its lowest ratio and increased gradually to achieve a desirable particle that performs well in both dynamic and light scattering categories.

With the assessment of the particle complete, two seeding challenges arise. First, as both studies focus on the separated flow region there must be an initial supply of seed particles present. Introducing the seed with the flow will promise good tracking in the freestream flow but fail to capture enough particles in any recirculation areas. A priming technique is applied where the seeder fills the settling chamber until the seed is visible in the test section as shown in figure 2.8 for the finned heat exchanger. The presence of particles throughout the test section ensures that there will be enough particles per interrogation region to effectively determine the velocity during the cross-correlation method. Priming the settling chamber also addresses the second challenge of continuous particle density in the flow. As the PETAL test facility exhaust its airflow to an external tank, there is no ability to recirculate the particles for a constant homogenous mixture through the test section. Priming the settling chamber with seed acts as a reservoir tank to ensure an evenly distributed number of particles for the duration of the image acquisition.

Figure 2.8 Smoke Generated at No-Flow Conditions over the Baseline Fin Design

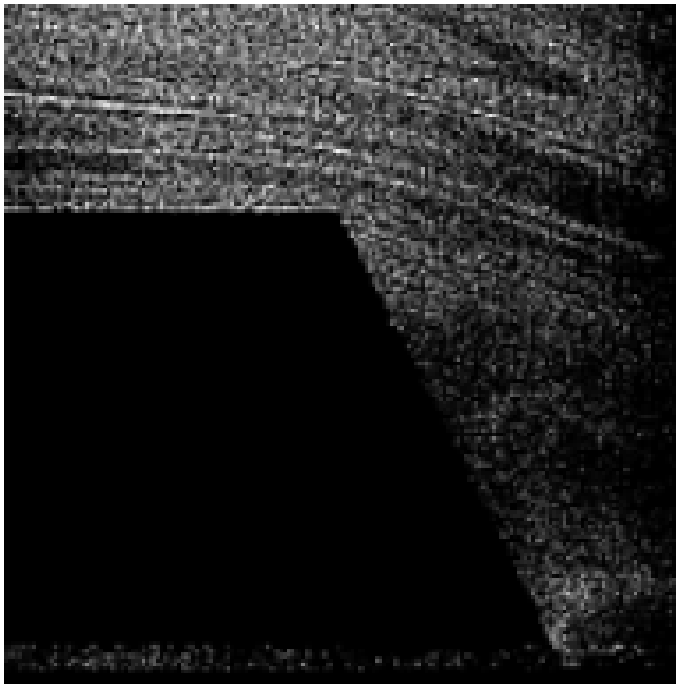

Figure 2.9 Image of Primed Particles at No-Flow

At no-flow conditions, the seed is observed in the test section and indicates that the settling chamber is primed. This does not imply that the entire settling chamber is filled with seed particles as this fill time would take significantly longer and yield diminished returns. As the seeder heats the particles to approximately 370º F into the ambient settling chamber, there is a risk of particle agglomeration resulting in a particles size much larger than designed. Imaging

of the primed particles shows consistent particle size at the region of interest in figure 2.9. Note that the particles are sparser at the trailing edge of the heat exchanger channel when compared to the freestream region. While this reduces the spatial resolution in this region, the density is sufficient to perform the measurement. Another aspect to note for the oil based seed used in this setup is the lack of smearing that occurred on the test section windows. As mentioned in the first section, there is risk of the seed collecting and reducing the quality of the images acquired. While the test section was fully primed, no streaking or agglomerates of oil were visible on the windows; supporting the decision to use an oil based seed.

The setup for the seeder is depicted below to the global seeding port just downstream of the fast-actuating valve. The seeder is controlled through the Control Room's virtual interface via a relay switch to open and close the nitrogen inlet valve. The nitrogen is fed to the seeder's inlet valve from the test cell's nitrogen panel. The outlet of the seeder is connected to a global seeding port just after the fast-actuating valve of the settling chamber. A custom designed rake is inserted into the 10in pipe before the settling chamber where the seed particles are introduced parallel to the flow. The ViCount Smoke generator has a pressure range of 270psi with a maximum differential pressure of 80psi. The smoke generator can produce a sustained smoke density and particle diameter for several hours at a rate of 0.85g/s. A 10in seeding rake is installed inside the inlet pipe to the settling chamber. The seeding rake directs the particles downstream paraxial with the flow to prevent any choking at the rake. This allows for a uniform mixing with the airflow taking advantage of the settling chamber's radial discharge identified in figure 2.2.

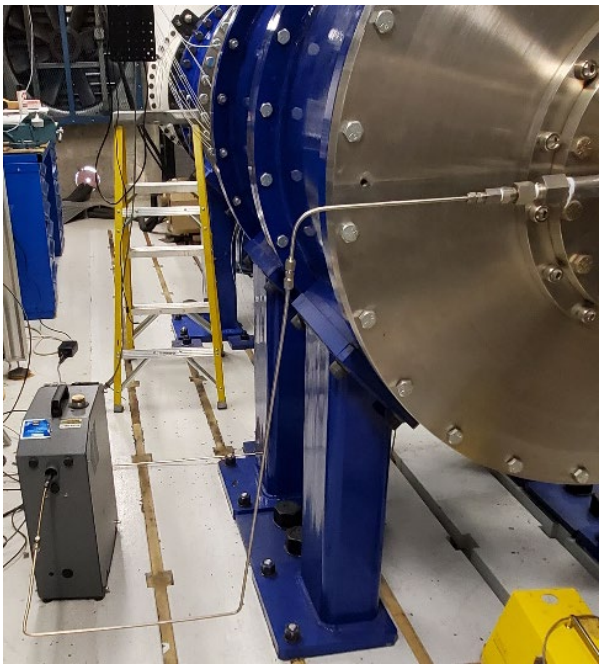

Figure 2.10 Global Seeding Configuration

2.3 Optimization of the Optical Setup

In both studies, the laser is guided to the top of the test section and enters through the middle window seen in figure 2.3. Figures 2.11 and 2.12 depict the optic train and camera setup. The laser's path is highlighted in green to show the function of the optic train to enter the test section from the top window. To reduce reflections in the finned heat exchanger tests, matte blue tape is set on the far side wall behind the fins. For both the heat exchanger and the hump the test articles are coated in a non-reflective graphite spray. While this spray proved effective in reducing reflections from the laser, the coating eroded from small areas and some reflections begin to appear in later test runs.

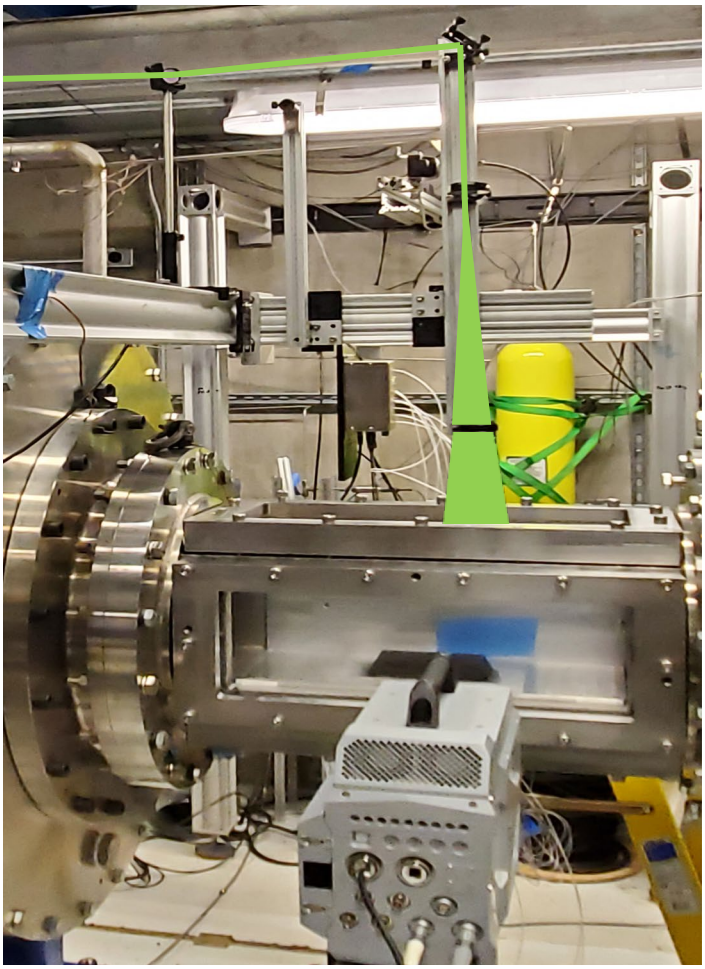

Figure 2.11 Optical Setup for the Finned Heat Exchanger

For the wall-mounted hump, the light sheet entered the test section at an angle to reach the desired region of interest starting at the crest of the hump. An optical rail mounted at 45º enabled the light sheet to properly enter through the window without clipping the sheet. This position loses the ability to measure the flow above the crest but is still able to capture particles downstream of the port injections.

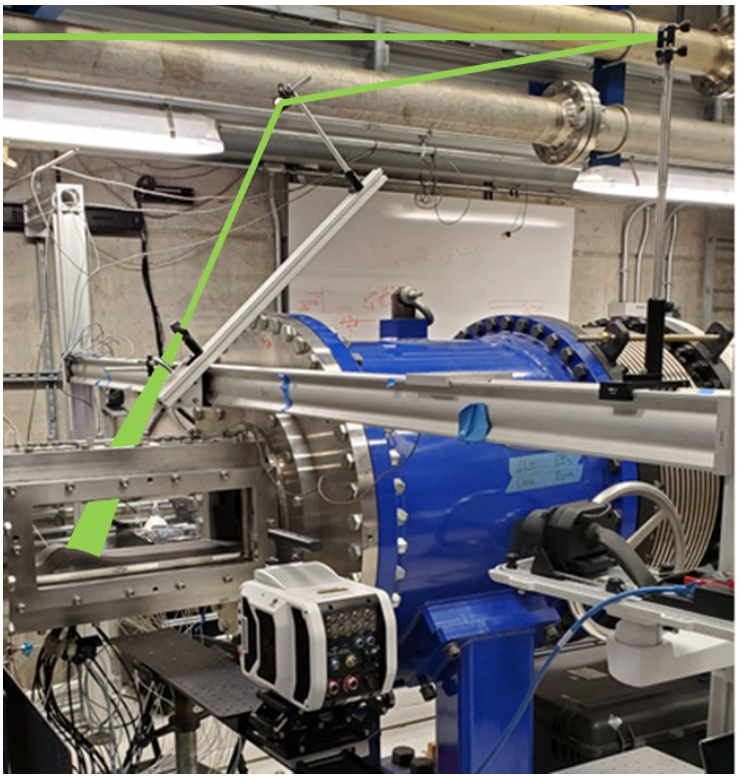

Figure 2.12 Optical Setup for the LPT Wall-Mounted Hump

An Nd:YAG laser with 532nm wavelength, λ, and a 20 kHz sampling rate for a 10ms pulse-burst created a light sheet through a –100mm cylindrical lens and a 400mm spherical lens. For the heat exchanger, the spherical and cylindrical lenses were positioned to create a light sheet that achieved a region of interest of 30.3mm. This sheet height is determined through the back focal length of the lenses given the distance between them as defined in the below equations.

$$d_B' = \frac{d_B(f_1 - d)}{f_1} \tag{4}$$

$$BFL_{top} = f_1 - d \tag{5}$$

$$BFL_{side} = \frac{f_1(d - f_2)}{d - (f_1 + f_2)} \tag{6}$$

$$Height = d_B' \left(1 + \left(\frac{bfl_{top}}{bfl_{side}}\right)\right) \tag{7}$$

$$t = \frac{d_B}{f_2} * \frac{H}{2} \tag{8}$$

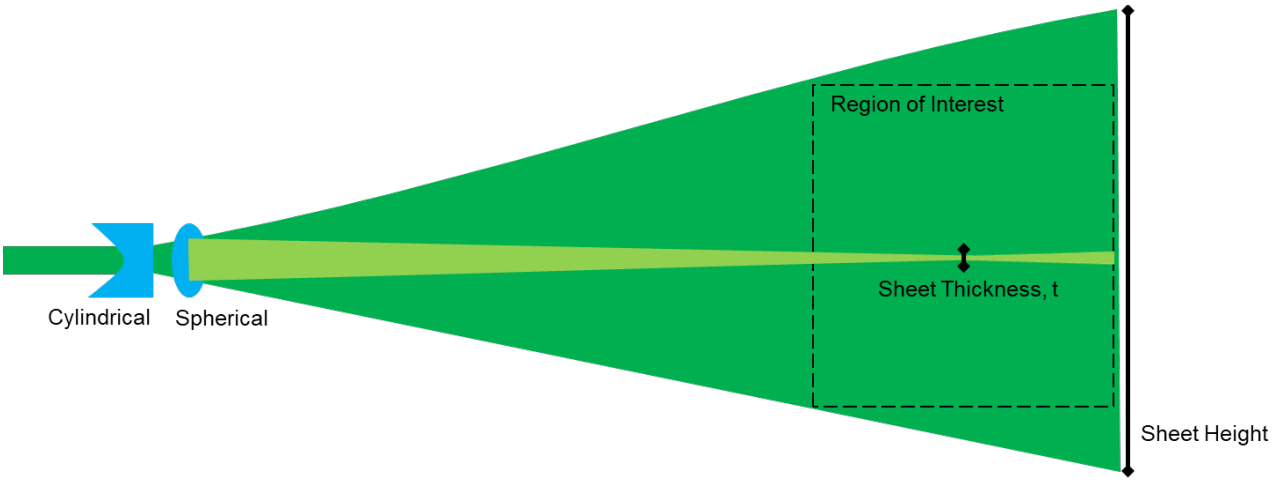

Figure 2.13 Graphical Depiction of the Light Sheet

The equations above and figure 2.13 show how the focal length of the cylindrical and spherical lenses and the distance to the region of interested determine the height of the light sheet. There are few other configurations to achieve a light sheet using diverging lenses or the addition of a third lens to maintain a constant sheet height or thickness [1]. One setback to creating a larger light sheet is the reduced intensity towards the edges as the laser follows a gaussian curve. The highest intensity, and brightest region, of the light sheet is located at the sheet thickness, t. It is beneficial to determine this location as this may produce brighter particles relative to the surrounding particles in the region of interest. Applying a third optic to maintain a constant thickness or adjusting the spherical lens to change the light sheet's center will aide in a more uniform light sheet with fewer image processing demands later.

To reduce variations in light intensity between image pairs, an oscilloscope is also used to adjust the gain on the laser pulses resulting in a pulse width of 3ns and 13ns for the pulse pairs. An example of the raw image pair for the baseline fins is shown below to show similar light intensity between the two images.

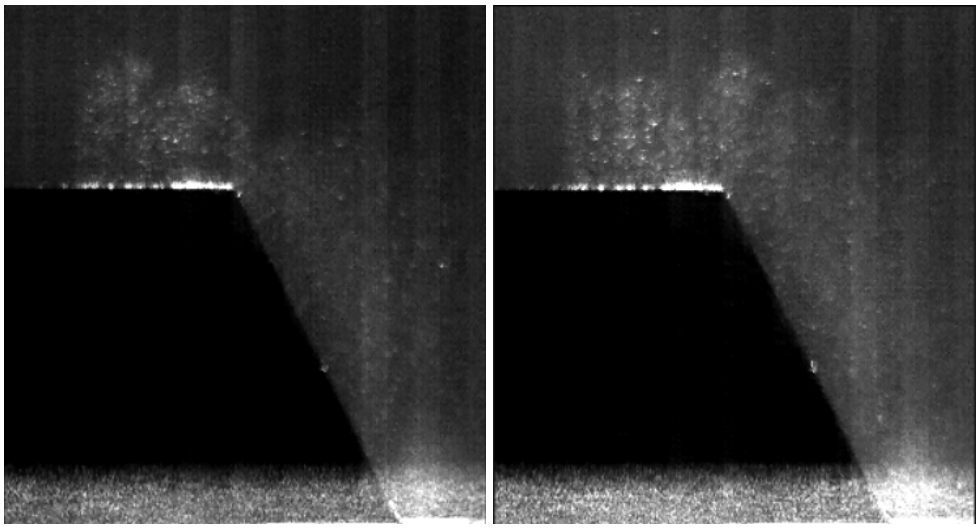

Figure 2.14 Raw Image Pair for the Baseline Finned Heat Exchanger

An oscilloscope is also used to confirm the synchronization of the laser and camera. For the finned heat exchangers, a Photron SA-Z high-speed camera is synchronized to the laser's onboard delay generator records the 10ms laser burst at 20 kHz. The camera is triggered from the laser to employ the frame straddling technique for single exposure, double frame PIV. For the wall-mounted hump, the same synchronization technique is applied, but with a different pulse-burst laser and high-speed camera. The second laser system used provided a similar performance with little difference in light intensity between pulse pairs with an identical pulse width set to 10ns each. The high-speed camera used for this second study is a Phantom v2012. This camera has a pixel size of 28μm and a sensor length of 1280x800 pixels. The added benefit to the Phantom is the PIV mode embedded in the software. Beyond the standard frame straddling technique, this camera allows the user to execute a pulse burst of frames based on the user inputs for number of bursts and time between frames.

The camera parameters are optimized to provide a high dynamic velocity range and dynamic spatial range from the images. A 50mm lens is used on the Photron SA-Z, and the optimized magnification and f/#, or aperture, are determined using the equations below. The sample size, c_r, describes the diameter of the particle image in pixels. A typical range for the sample size is between 1 to 3 pixels. Outside of this range results in under or over sampling the particle image. It is determined by Adrian that a c_r larger than 3 has diminishing returns in reducing mean bias error or random error [6]. The Photron SA-Z has a pixel resolution, d_r, of

20μm and a pixel length of the camera sensor of 1024x1024 pixels. This provides a sensor length of 20.48mm. The depth of field, δ_z, defines the thickness of the region for in-focus particles. A depth of field is applied to reduce the loss of out of plane particles in an image pair.

$$M_{opt} = \frac{c_r d_r}{\sqrt{(1.5*\delta_z*\lambda)+d_p^2}} \quad (9)$$

$$f\#_{opt} = 0.5 * \frac{\sqrt{\frac{\delta_z}{\lambda}}}{\left(1+M_{opt}^{-1}\right)} \quad (10)$$

$$d_s = 2.44 * f_\# * (M+1) * \lambda \quad (11)$$

$$d_\tau = \sqrt{(M * d_p)^2 + d_{diff}^2} \quad (12)$$

$$DVR = \frac{c_{max}}{c_\tau\sqrt{1+c_r^2}} \quad (13)$$

$$DSR = \frac{L_x/M_{opt}}{\Delta x_{p,max}} \quad (14)$$

The DVR is found using the particle pixel diameter, the maximum distance travelled, c_{max}, and constant, c_τ, which determines the ability to find the particle displacement between images and typically ranges from 1-10% of the image diameter. The maximum distance the particle travels, c_{max}, follows the "1/4 Rule" recommended by Adrian [6]. This rule explains that the particle should not travel further than one-quarter of the initial interrogation window. A value of 16 pixels is then used to correlate to an initial interrogation window of 64 pixels. After this initial pass in the cross-correlation method, refined interrogation windows can be introduced with an initial pixel shift based on the first pass. These subsequent passes improve accuracy of the velocity as well as resolve the velocity field closer to the allowable spatial resolution. The dynamic spatial range is a product of the camera sensor's length, the resulting optimized magnification, and the displacement of the particle. As the DSR relates to the field of view of the image to the particle displacement, a shorter delay between laser pulses improves the spatial range of the image. This shorter delay, however, impacts the DVR as the ability to resolve the smallest particle shift diminishes. Optimizing the field of view of the image is the preferred method for improving the spatial range without affecting the resolvable velocity range. The final

dynamic velocity range and dynamic spatial range are seen in the table 2.2 for the two cameras used.

Table 2.2 Optical Optimization Parameters

Inputs						
c_r [px]	d_p [um]	δ_z [mm]	λ [nm]			
1	1	30/4.2/4.8	532			
Photron [Baseline/Optimized Heat Exchangers]						
$d_{s/diff}$ [um]	d_τ [um]	d_r [px]	M_{opt}	$f\#_{opt}$	DSR	DVR
20	28.2	20	0.13/.34	14/11	64/32	226
Phantom [LPT Wall-Mounted Hump]						
$d_{s/diff}$ [um]	d_τ [um]	d_r [px]	M_{opt}	$f\#_{opt}$	DSR	DVR
28	39.5	28	0.45	14	26	226

Table 2.2 shows the final outputs for the defined parameters for both cameras. Initially, an optimized magnification for this experiment is 0.4 with an f/# of 11 for the finned heat exchanger study. This yields a diffraction limited spot size, d_s or d_{diff}, of the particle as 20μm, which agrees with a pixel diameter, c_r, of 1. A pixel diameter of 1 is chosen for this measurement to achieve a larger DVR given the flow conditions. The recorded particle image diameter, d_τ, is 28μm. This image size is larger than the camera's pixel resolution and avoids peak locking.

During the setup, the pulse-burst laser was switched from doublet to singlet pulse as the high-speed camera could not support the shorter time between frame pairs. This results in a larger pixel shift of the particle in the image, and negatively impacts the dynamic spatial range. While particle tracking is still feasible in these images, the DSR must be improved. Modern commercial cross-correlation methods such as LaVision's DaVis employ what is known as an initial pixel shift during the first pass of the interrogation window. This can account for larger pixel shifts and enable the use of a smaller interrogation window – 64-by-64 pixels rather than 256-by-256 pixels – all while maintaining the "1/4 Rule". This fixed DSR for the finned heat exchangers is updated in the table above. During the baseline heat exchanger setup, the camera is placed further away from the test section due to physical constraints of vibrations. To account for this change, a magnification of 0.13 and f/# of 14 is used to maintain proper focus on the light

sheet. While the optics set up improved spatial resolution, the increased depth of field captured more out of plane particles. With an increase in the depth of field, this can result in the inclusion of out of plane particles in the image adding noise to the image. The camera position is fixed for the optimized heat exchanger as well as the wall-mounted hump. A reduced depth of field around 4-5mm is used and reduces the risk of added noise in the images. The wall-mounted hump experiment utilized a different camera that can support the doublet pulse pairs from the laser. The doublet pulse pairs allowed for greater particle tracking and an improved DSR without the assistance of an initial pixel shift during the cross-correlation method. The improved DSR is observed in the table above.

The images were calibrated using a Dantec calibration plate with a dot diameter of 5mm and a distance between two dots of 40mm. The plate provides three dimensional capabilities with a recessed plane of dots between the primary plane. The resulting pixel scale for the baseline and optimized fins is 7.38px/mm and 2.289px/mm. The wall-mounted hump calibration yielded a pixel scale 2.22px/mm. Prior to testing, background images were taken for each fin design with and without the laser light sheet. This assisted in reducing reflections and any reflections from the acrylic window on the test section.

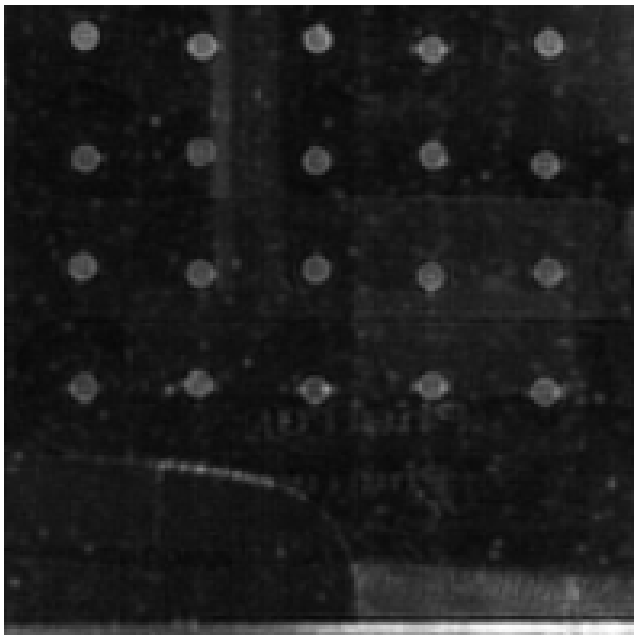

Figure 2.15 Calibration Images of for the Optimized Finned Heat Exchanger

2.4 Uncertainty Quantification

While the optical optimization above ensures good spatial and velocity resolution, there still exists a measurement error in the recorded images. The optimization of the magnification assists in reducing this unknown error and avoids loss in resolution. Another rule is established where the imaged particle diameter, d_e, is set just equal to the pixel size of the camera. This ensures the lowest magnification required and prevents any under or oversampling of the image. The error associated with PIV measurements is in part due to the unknown location of the particle's center in its image. The inherent noise in electronically recorded images make it difficult to determine the true center of the imaged particle. For both test cases, it can be assumed that the uncertainty in the Δt between laser pulses is negligible [6]. An equation for the rms error in the velocity measurement is defined:

$$\sigma_u = \frac{\sigma_{\Delta x}}{\Delta t} = \frac{\sigma_{\Delta X}}{M_o \Delta t} \qquad (15)$$

$$\sigma_{\Delta X} = c_\tau d_\tau \qquad (16)$$

Where $\sigma_{\Delta x}$, is the error measurement of the particle in the fluid and $\sigma_{\Delta X}$, is the error of the image particles displacement. Calculating $\sigma_{\Delta X}$ is accomplished by the constant c_τ and d_τ defined above in table 2.2. Figure 2.16 depicts the relation between these two variables in finding the centroid of the particle in the image. From this drawing it is clear how a small pixel to sub-pixel shift of the true center of the particle can impact the actual displacement of the particle and its direction of travel.

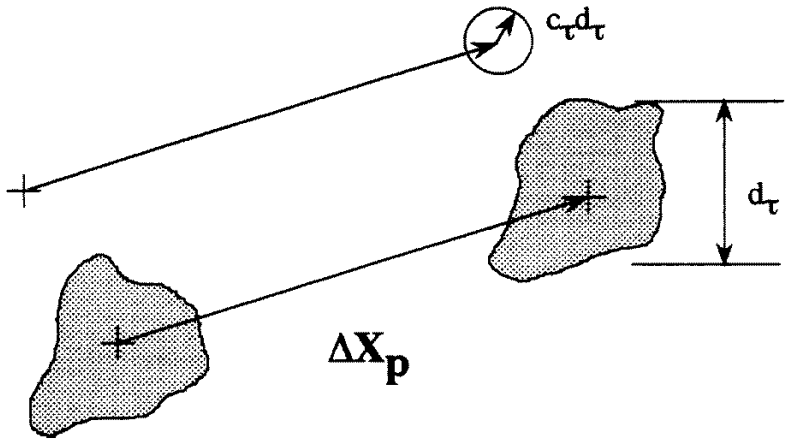

Figure 2.16 Measurement Uncertainty in the Imaged Particle Displacement [6]

From equations 15 and 16, the displacement and velocity errors are found. The low errors for both test cases in table 2.3 are due to subsonic flow conditions allowing for a relatively longer time between pulse pairs. A longer Δt increases the dynamic velocity range for the measurement system while reducing the error in the velocity measurement according to equation 15. The particle travels further in the fluid and if maintained to the "1/4 Rule" and applying subsequent interrogation windows, a smaller velocity can be resolved. The set back of increasing the pulse delay is the reduced spatial range. While the "1/4 Rule" may be maintained, a larger maximum pixel shift and interrogation window are required in the first pass of the cross-correlation method. This larger shift in pixels closer to the maximum velocity results in a larger window average the in the resulting vector field. To show this, the table below shows the finned heat exchanger study with the designed doublet pulse and the measured singlet pulse from the pulse-burst laser. Note that the doublet pulse pair with a shorter delay has an increased error for the velocity measurement.

Table 2.3 Displacement and Velocity Errors

	c_τ	d_τ [μm]	$\sigma_{\Delta X}$ [μm]	Δt [μs]	M_o	σ_u [m/s]
Heat Exchanger Design	0.05	28.2	1.41	4	0.34	1.02
Heat Exchanger Measured	0.05	28.2	1.41	50	0.13	0.22
LPT Hump	0.05	39.5	1.98	9	0.45	0.49

With the optical setup the same for both cases of the heat exchanger, the change in delay between the pulse pairs shows a significant impact on the accuracy of the measurement. Note that the particle image displacement error is identical out to a magnitude of $1x10^{-12}$m for these two cases. As this error is based on the optical resolution of the measurement system changes in the magnification can make an effect if the magnification is changed to a scale where the diffracted particle diameter is smaller than the pixel size of the camera.

In a later section, the velocity measurement uncertainty will be compared to the uncertainty quantifications from LaVision's DaVis 8 software. This software provides image processing tools as well as customizable cross-correlation methods. These features as well as the statistical analysis tools are used to assess the methodology. The error measurements above will be compared to DaVis 8's correlation statistics-based uncertainty to see if the uncertainties determined prior to the experimentation are a good predictor for the accuracy of the results.

3 EVALUATION OF THE PIV MEASUREMENT SYSTEM

3.1 Experimental Methodology

For both test cases, a mass flow is set from the virtual interface in the control room to set conditions prior to admitting the flow into the test section. The test sequence allows for the correct mass flow through the venturi with the purge valve open. During this time, the smoke generator is open to allow for a priming of particles into the settling chamber. Once the mass flow was met, the flow mixes with the seed in the settling chamber and passes through the test section. The testing procedures for the PIV measurement is dictated by the duty cycle of the pulse-burst laser. For the finned heat exchanger, the pulse-burst laser used required a cooling period of 10 seconds for every 10ms burst. The second laser used during the wall-mounted hump campaign required only a 4 second cooling period for every 10ms burst.

This sequence is manually timed such that at t+5 seconds the flow is introduced into the test section, and at t+8 seconds the camera is placed in ready mode to receive the trigger from the laser's delay generator. At t+10 seconds the laser fires a 10ms burst at 20 kHz equating to 200 frames, or 100 image pairs. The change in intensity of the light sheet near the beginning and end of the 10ms burst for the first laser resulted in 76 usable images while all 100 image pairs of the second laser showed a normalized intensity from beginning to end.

With full capacity of the air tanks during the finned heat exchanger testing a total of six measurements are captured. Further iterations were conducted, however, due to the cooler temperature of the air, the heated smoke began to cool once mixed in the settling chamber resulting in sparse particles appearing in the region of interest. Future experiments will employ heated air to maintain ambient temperatures and prevent any congealing of the smoke particles. For the wall-mounted hump, a total of 18 iterations are measured. With the shorter duty cycle of the second laser, three measurements are taken for each case. Measurements for the baseline, no blowing from the injection ports, and blowing are measured at the opening of the fast-actuating valve, during the middle of the iteration, and after the valves are closed.

3.2 Particle Analysis

The images below compare the raw to processed image for the baseline and optimized finned heat exchangers. Note that the vertical lines in the background of the first image are from the matte tape on the far wall. While the seed particles show a strong light scattering effect in the raw image, the density of the smoke creates severe noise in the image. A background subtraction is done to remove the image of the tape and excess reflections at the base of the fins. Further, a sliding average is applied to increase the signal-to-noise ratio and extract particles near the trailing edge of the fins. The second image below shows the resulting image ready for cross correlation. The base of the fins still suffers from reflections and approximately 3.4mm from the hub is lost.

The optimized fins produced similar results in the raw images, however, the images experienced more saturation in the middle of the light sheet. This higher intensity in the middle of the sheet may imply that the focal length of the spherical lens is present in the image. The background subtraction was able to account for this saturation without significant loss of particles in the images. After removing the 12 images at the beginning and end of the 10ms laser burst, the 76 remaining images showed consistent intensity. Additionally, with the assistance of adjusting the pulse width for the laser doublets, the image pairs show consistent intensity with no need for normalization across the set.

The 100 image pairs from the wall-mount hump measurements showed consistent light intensity. As testing progressed, the graphite spray eroded downstream of the port injectors where severe reflections are present in the raw images. Background subtraction of the light sheet with no flow or seed is used to eliminate majority of the reflections.

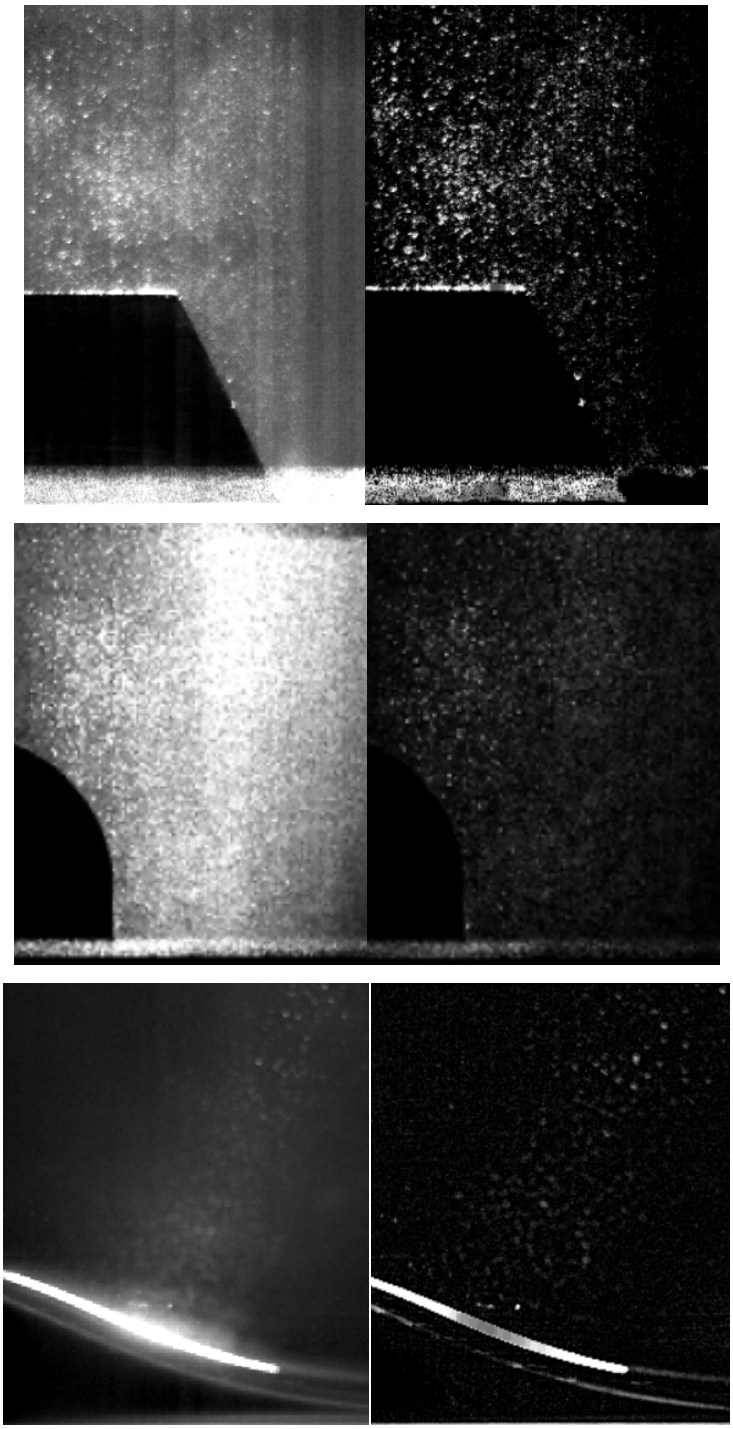

Figure 3.1 Comparison of raw and post-processed images

The resulting particle size in the heat exchangers is on average one pixel in diameter, however, clusters of particles made it feasible to track from frame to frame to confirm an accurate tracking and pixel shift. While a c_r of 1 pixel in diameter is chosen for both studies, the

image particle is expected to be slightly larger than the pixel size of the Photron SA-Z camera to avoid any peak locking. The resulting particle from the seeder may be smaller than designed which would result in the smaller diffraction diameter. This is supported by the intensity of the average particle when compared to the particles in the wall-mounted hump. The intensity of the particles in the heat exchangers is on average 800 with a background average of 193 whereas the wall-mounted hump showed a particle intensity of 2000 on average with a background of 257. The particles in the wall-mounted hump showed a larger than calculated diameter of 5 pixels. With this actual image size, the new displacement error is 7μm with a velocity error of 3.24 m/s. Although the particles in this later study are larger, they remain small enough with a consistent density to employ a refined 16-by-16 pixel interrogation window during the multipass cross-correlation. Figure 3.2 shows the shift in one image pair for the wall-mounted hump.

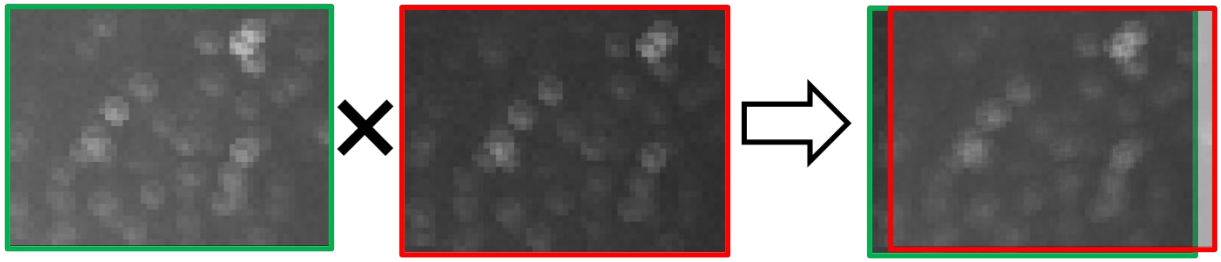

Figure 3.2 Tracking Particle Motion in one Image Pair

Images from the PIV testing were calibrated, processed, and cross-correlated using LaVision's DaVis 8 software to analyze the velocity profiles. For the cross correlation, LaVision's DaVis 8 software is used to calculate the vector fields and resulting plots. The images are imported with camera attributes for a single camera, double frame configuration to account for the 20 kHz sampling rate with a Δt dependent on the iteration ran as mentioned in table 2.3. The algorithm used consists of an offset in the x-direction based on the anticipated pixels traveled in the time between pulses. This allows for sub-pixel calculation and a more accurate vector field. The technique applied followed a time resolved cross correlation using double frames (1+2, 3+4, 5+6…) with multipass iterations for an initial interrogation window of 48 pixels for the heat exchangers and 64 pixels for the wall-mounted hump at 50% overlap, and three passes at 16 pixels at 50% overlap. Vector processing is done to improve the accuracy of the vector field. During each pass, vectors are removed if they fall below a peak ratio of 1.3. This

reduces the noise from the images, however, for an image with substantial noise this results in removing potentially accurate peaks in the correlation map [1]. For the heat exchangers, the baseline and optimized fins show peak ratios of 6.67 and 3.12. For the non-blowing and blowing iterations for the wall-mount hump an improved peak ratio of 27.7 and 26.5 is determined. While the wall-mounted hump with blowing case has a higher peak, it is important to note that the peak is quite wide rather than displaying the typical sharp peak one would expect and may prove less accurate. The peak ratio relates the first two highest peaks in the resulting correlation map. The higher peak ratio observed in the wall-mounted hump study corresponds to the improved signal-to-noise ratio of the particles.

3.3 Assessment of Dynamic Spatial and Velocity Ranges

The resulting vector fields for each case is assessed for the number of vectors in the spanwise direction. Based on the regions of interest for each case, The resulting number of vectors are 105, 53, and 24 for the baseline and optimized heat exchangers and the wall-mounted hump. These values relate to the expected DSR in table 2.2 and is seen in the resulting velocity fields. The multipass feature of LaVision's DaVis 8 software in conjunction with the initial pixel shift allowed refined averaging down to a window size of 16-by-16 pixels. The figures below reflect the smoother gradient due to the improved dynamic spatial range despite the limitations of the CMOS camera explained by Hain [7]. Figure 3.3 shows the time-averaged velocity fields for the two finned heat exchangers and a non-blowing versus blowing iteration from the wall-mounted hump.

As the DVR was 226 for each design, the minimal resolvable velocity is less than 1m/s for the finned heat exchangers and around 1 m/s for the wall-mounted hump based on the expected freestream velocities for each case. As the number of vectors is doubled for the baseline compared to the optimized, a smoother gradient is observed in the separated region, and smaller gradients are observed downstream of the trailing edge just above the tip height as residual mixing between the freestream and shear layer occur.

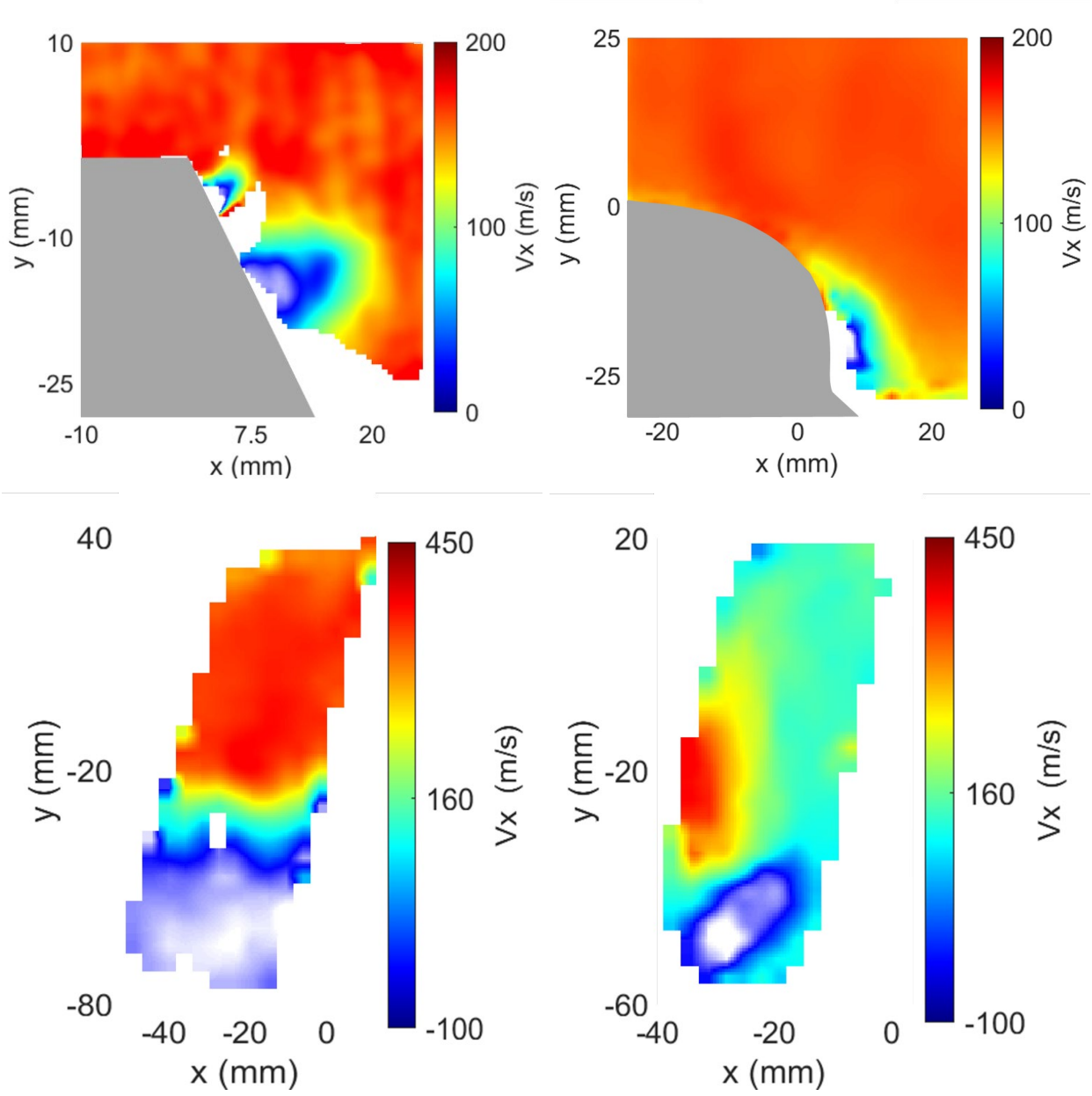

Figure 3.3 Time-Averaged Vector Fields for the Heat Exchangers (top) and Wall-Mounted Hump Without and With Blowing (bottom)

For the baseline and optimized heat exchangers, there are regions of no resolved velocities along the trailing edge. When reviewing the raw images, there is an inconsistency of particles in these areas that affect the correlation between images. This same assessment can be applied to the blowing and non-blowing studies for the wall-mounted humps. With no blowing, there is around 5mm from the surface of the hump to nearest resolvable velocity. As the DVR is

large enough to resolve down to 1 m/s in this experiment, the most likely cause for no correlation is a low density of particles in these areas or out of plane movement.

3.4 Flow Field Analysis

Velocity profiles in the x-direction are extracted from the time-averaged correlated image pairs and are compared to the CFD results in figures 3.4 and 3.5. CFD data for each geometry is provided by members of the PETAL team. The baseline results do not show data from approximately 10mm to the hub of the test article. This is due to limited particle presence in this region as well as reflections from the hub. The optimized fin results show data points 5mm closer to the hub. This may imply an improvement in performance from the optimized fins through boundary layer reduction. Both figures 3.4 and 3.5 include the uncertainty for the experimental data as calculated through LaVision's Davis 8.4 software which uses a correlation statistics-based method that quantifies uncertainty through the physical characteristics of the particle [6].

Velocity measurements are extracted in the spanwise direction for the finned heat exchangers at 5mm and 7mm downstream of the trailing edge and compared to CFD in the corresponding center channel of the heat exchangers at M 0.5. For the baseline geometry in figure 3.4 the PIV results show a larger separation bubble downstream of the fins, however, the spanwise location of the bubble is consistent with the CFD. At roughly 28mm in height, the CFD shows an increase in velocity towards the freestream value, $V_{x,\infty}$. The PIV experimental results show a transition to the $V_{x,\infty}$ at a shorter height of 25mm. The experimental results for the optimized fins seen in figure 3.5 show a stronger agreement to the CFD in both location and magnitude.

One reason for the disagreement between the modeled and experimental data is the location of the data downstream of a bluff body. The RANS CFD model will show discrepancies when presented with large gradients expected at the trailing edge of these geometries. With the improved design of the optimized heat exchanger, the more accurate matching at the freestream velocity shows a reduced gradient and therefore a better predictive model from the CFD.

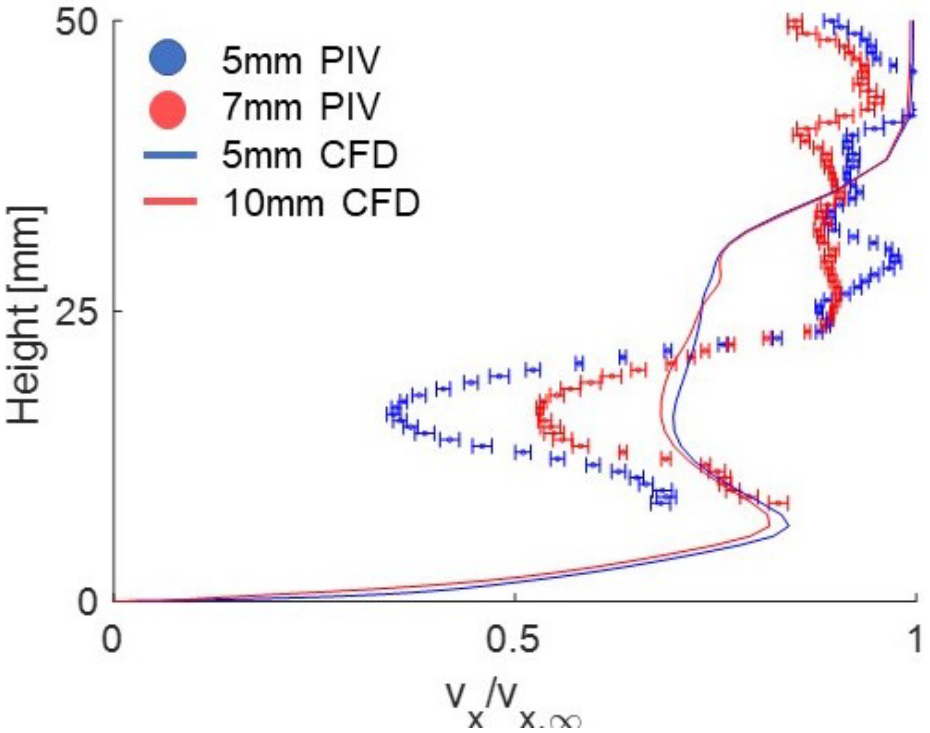

Figure 3.4 Comparison of Experimental and CFD Results for the Baseline Fins

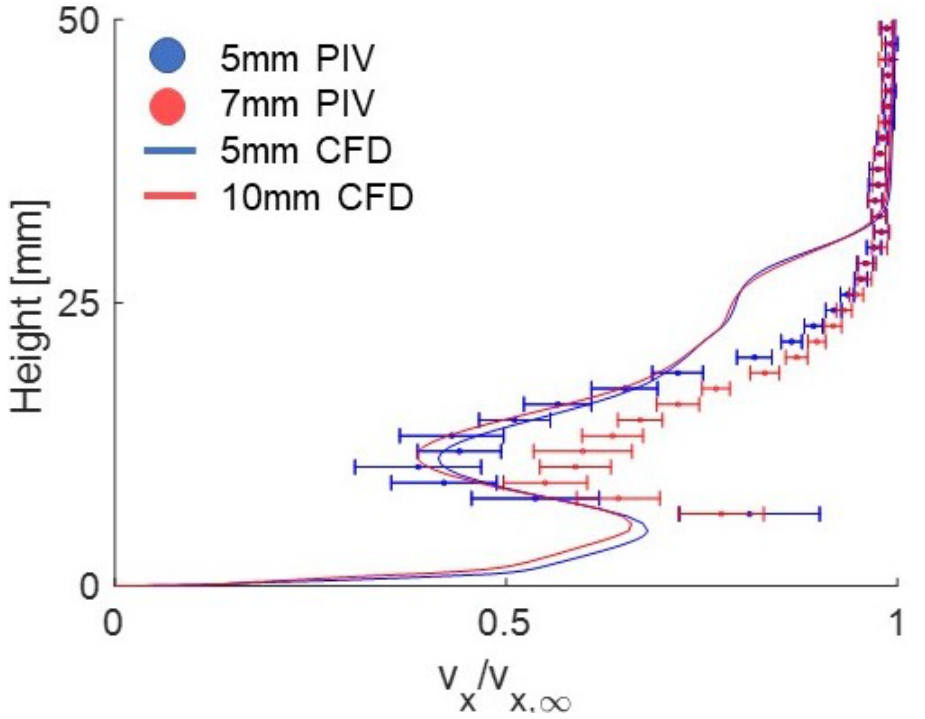

Figure 3.5 Comparison of Experimental and CFD Results for the Optimized Fins

The flow field analysis for the LPT turbine wall-mounted hump include comparison of instantaneous vector fields from the PIV results to Schlieren imaging and CFD provided by members of the PETAL team. The Schlieren images below depict the fully developed separated regions and are consistent for the final 5 seconds for the 10 second blowdown of the experimental iteration.

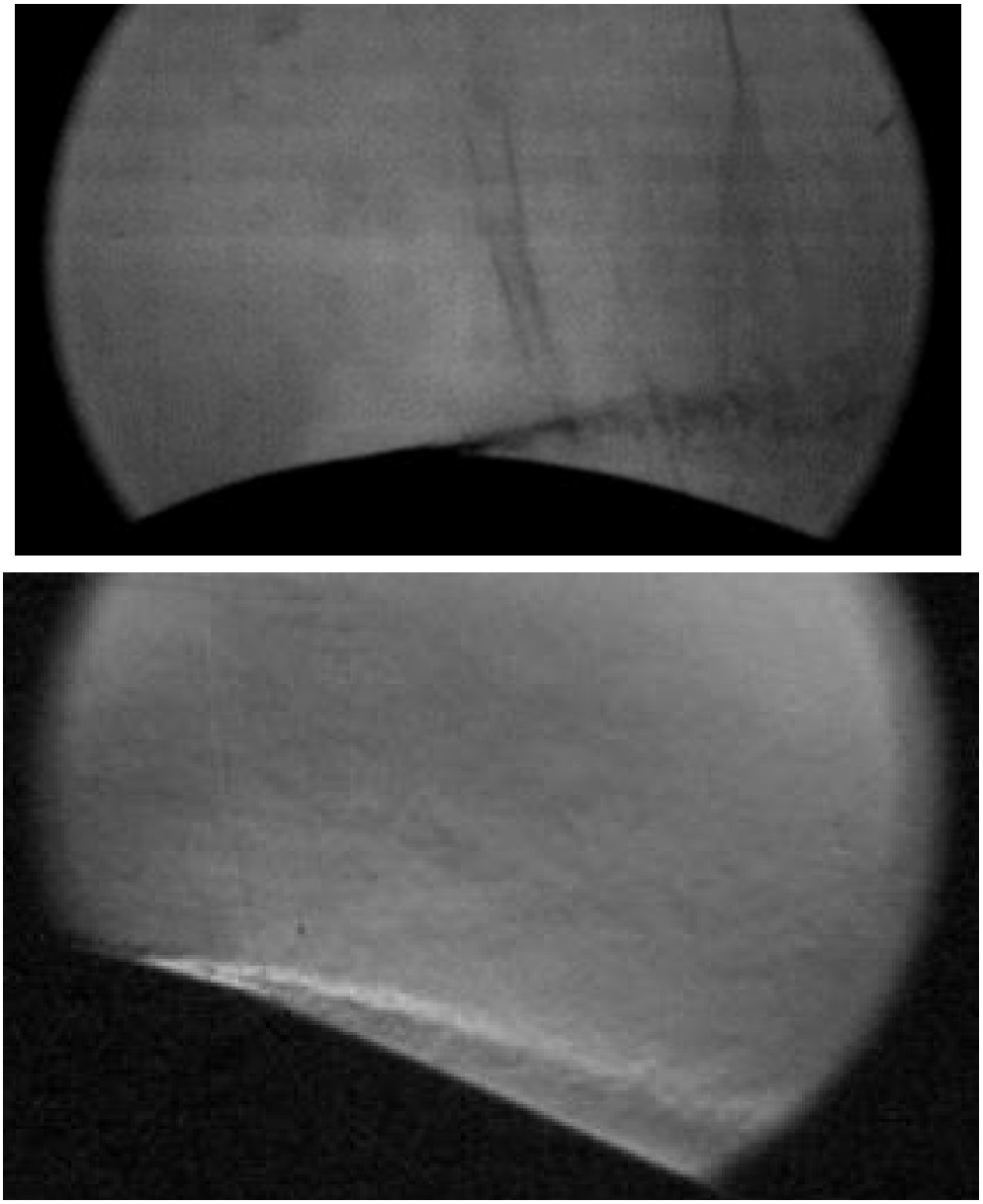

Figure 3.6 Schlieren Images of the Separation Layer Interaction without Injection (top) Injection (bottom) [5]

From the top image in figure 3.6, the separation layer begins at the crest and propagates further away from the suction side of the hump. This is consistent with the angle of the shear layer identified in the non-blowing vector field in figure 3.3. The instantaneous vector fields in figure 3.7 capture the development of the separated region for the 10ms sampling time. The height of the separation region fluctuates in the first four instances whereas little variation in height is seen between the last two profiles. Shedding can be seen in the shear layer between the freestream and separated regions. This unsteady behavior and the development of the large, separated region with no blowing explains the larger resulting gradient in the time-averaged vector field. This larger gradient is comparable to the fully developed gradient observed in the non-blowing Schlieren image above.

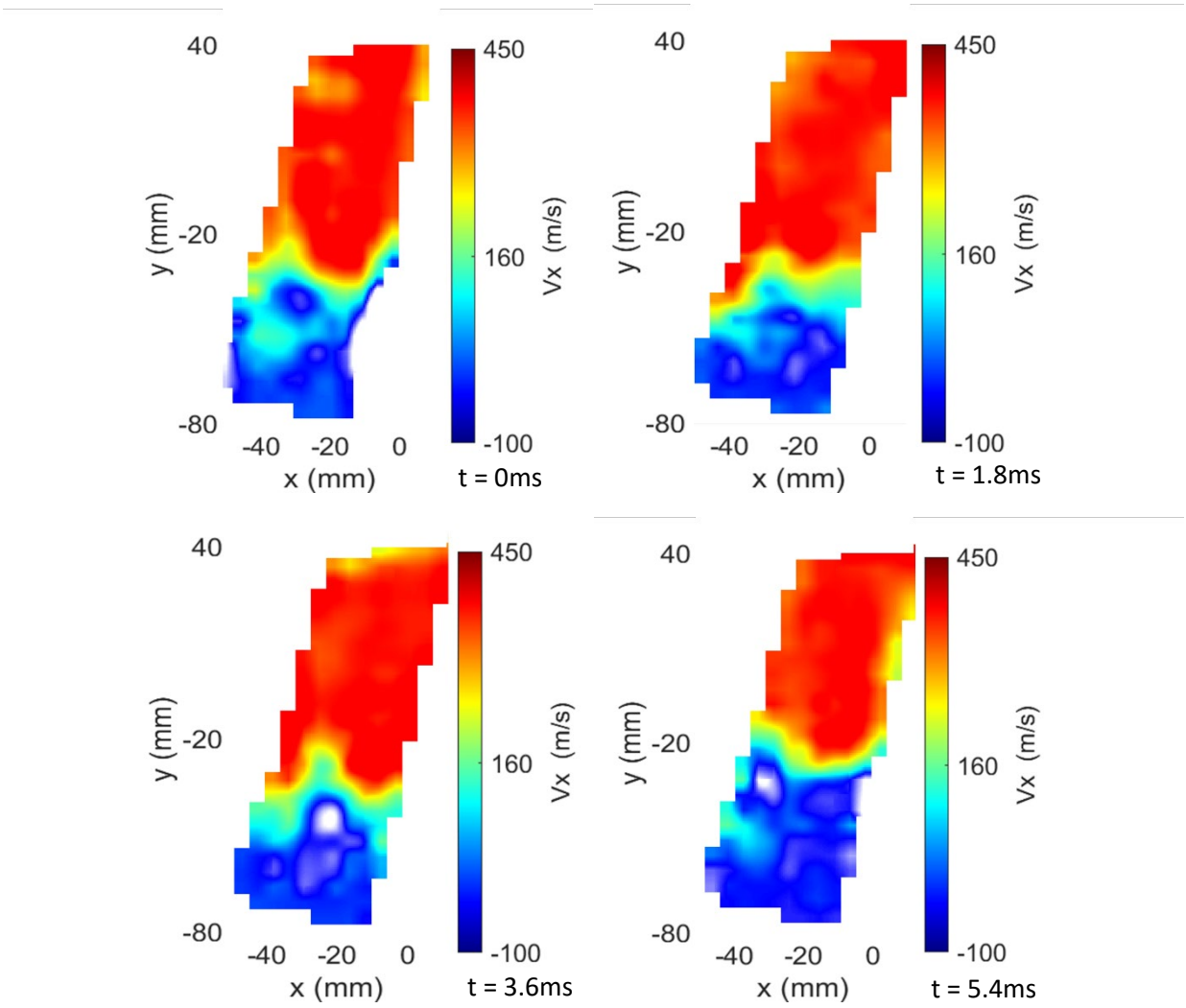

Figure 3.7 Instantaneous Vector Fields for the Non-Blowing Wall-Mount Hump

Figure 3.7 Continued

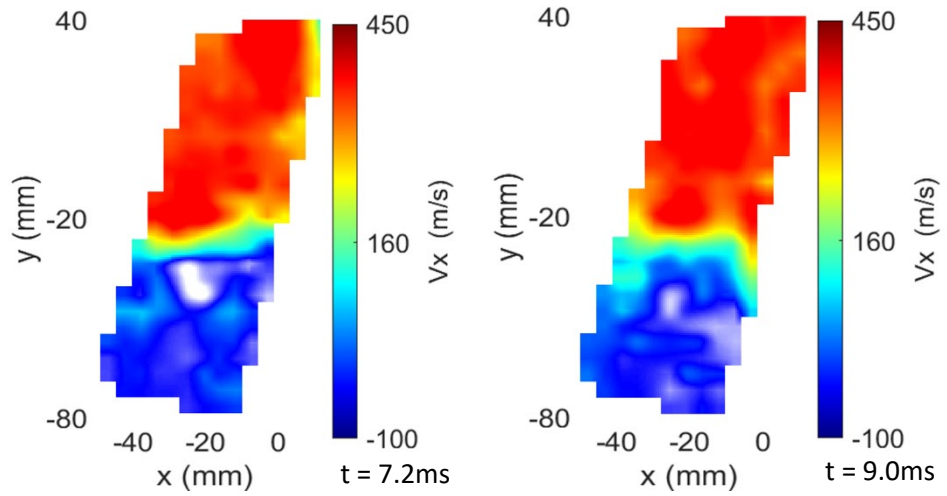

Looking at the instantaneous vector fields and the CFD model in figure 3.9 for the non-blowing case, there is substantial matching that is noted. The separated regions in both the experimental and modelled data is above the height of the crest. The CFD predicts a larger gradient for the shear layer between the freestream and separation bubble, however, from the instantaneous vector fields from the PIV, the shear layer grows larger as the flow develops.

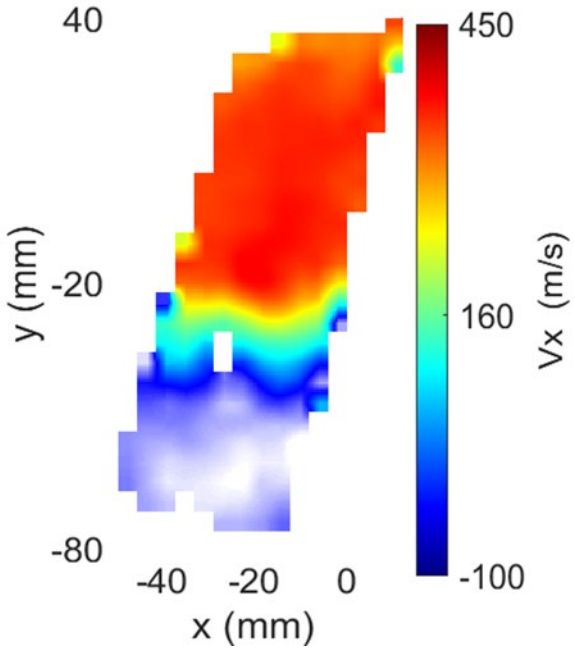

Figure 3.8 Time-Averaged Vector Field for Non-Blowing

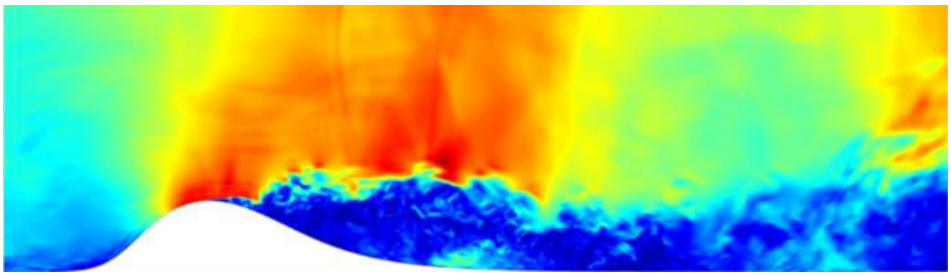

Figure 3.9 Mach LES Contours for Non-Blowing [5]

Moving to the wall-mounted hump with blowing, the bottom Schlieren image in figure 3.6 depicts the flow when the controlled blowing has successfully reduced the separation bubble. From the Schlieren data, this event takes place several seconds after flow is initiated. Based on the timing of the camera trigger, the resulting vector field shows the separation bubble as it still interacts with the controlled blowing less than one second into the experiment. Figure 3.10 shows the Schlieren image of the still developing flow and the interaction between the injection at the crest and the separation region. From the PIV vector fields in figure 3.11, a larger separated region is observed. The instantaneous vector fields seen here reflect this flow interaction as fluctuations in the separation bubble are observed.

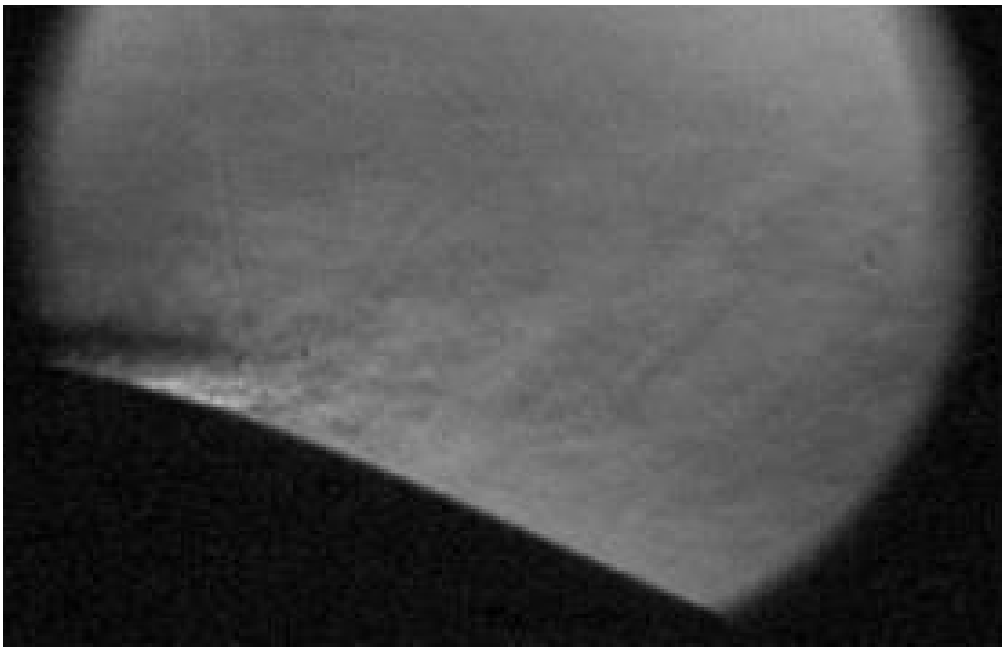

Figure 3.10 Separation Bubble Interaction with Blowing

When the flow becomes transonic in the test section, the strong shocks initially present at the leading edge of the port injection subside and the controlled blowing takes a greater control of the separation bubble. Over time, the controlled blowing weakens the shear layer. After roughly 4 seconds the controlled blowing maintains a shallow separated region as seen in figure 3.6 for the remainder of experiment. For the 10ms sampling time for the PIV, the blowing has not yet fully reduced the separated region which explains the fluctuations in height of the shear layer.

With the establishment of the separated region in the wall-mounted hump, the density of particles becomes very sparse with no ability to inject additional particles into this area. While priming the test section with seed provided resolvable data for the initial measurement, subsequent measurements after the 4 second cool-down time of the laser showed poor correlation due to the diminished seed density. Compared to the blowing instance, the vector field lies closer to the surface of the hump. This implies that the particle presence is stronger in this region when blowing is applied because the separated region lies closer to the surface when compared to the non-blowing case. The blowing from the injection ports improves the performance of the LPT turbine as there is a reduction in the separation layer. The results of the vector fields agree with the Schlieren taken of the wall-mounted hump with and without blowing.

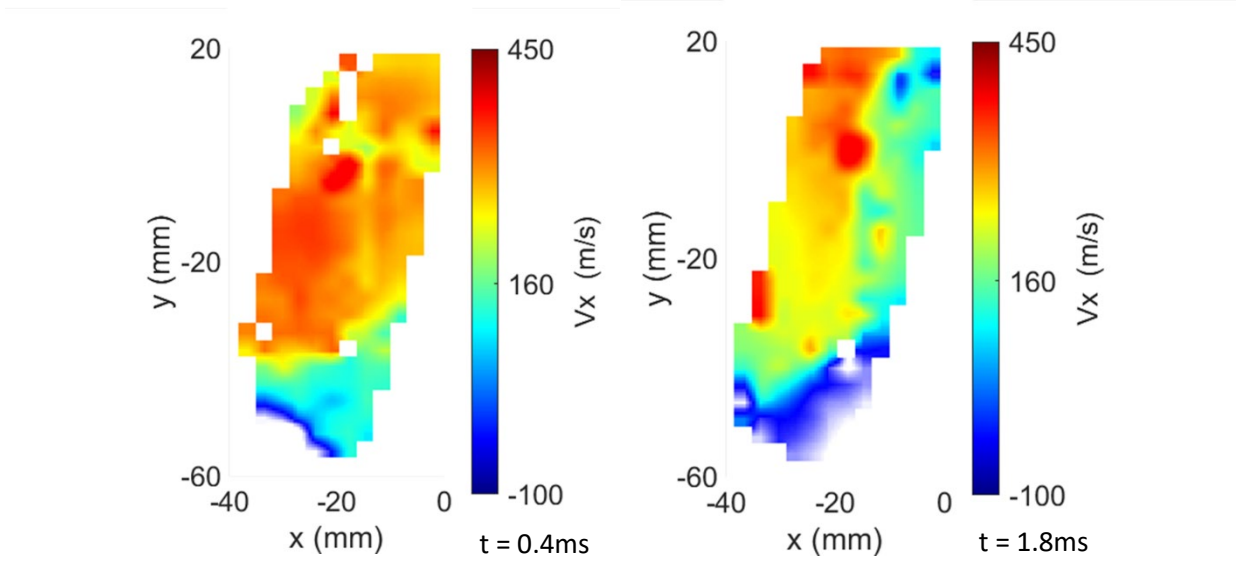

Figure 3.11 Instantaneous Vector Fields for Blowing

Figure 3.12 Continued

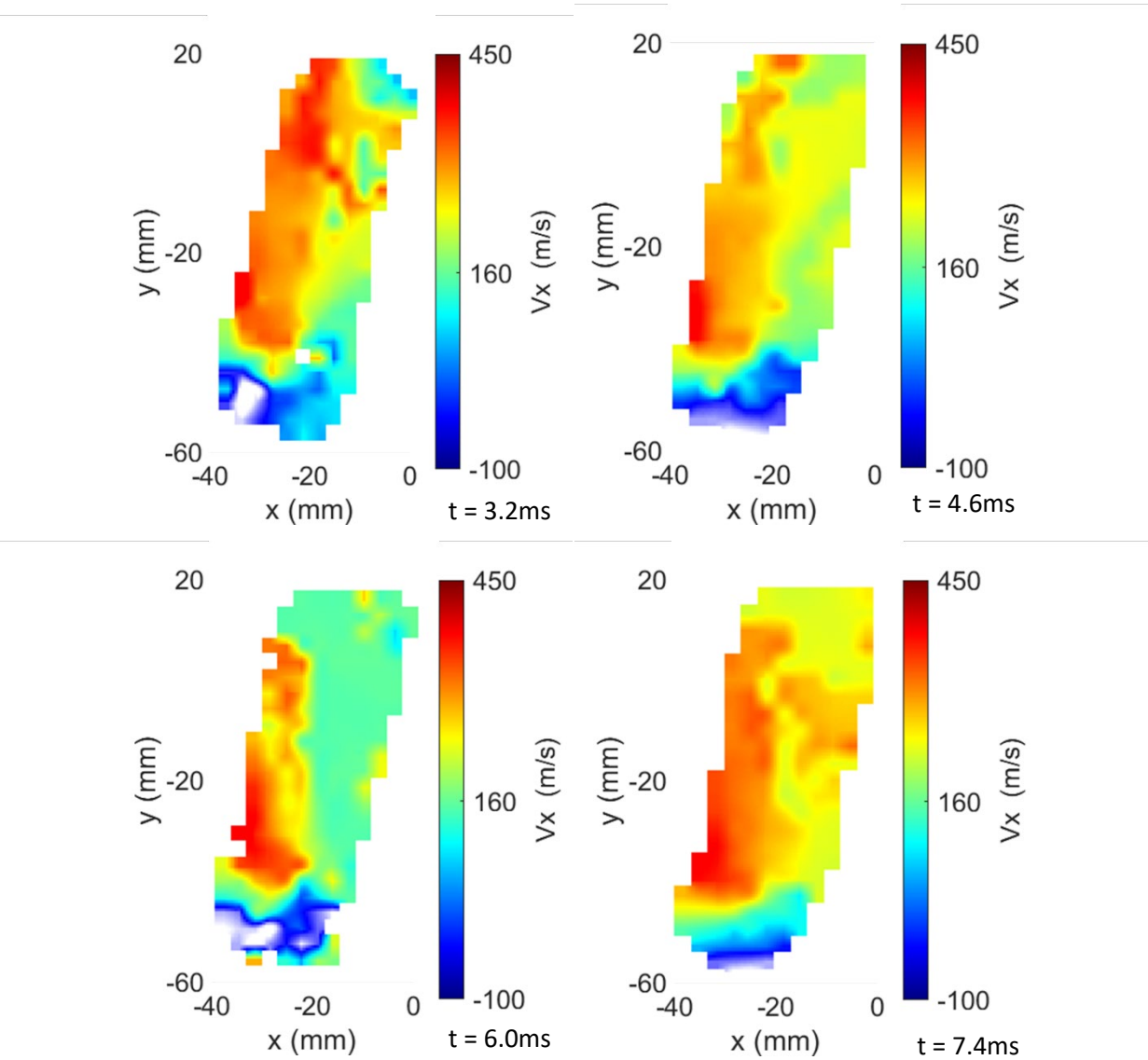

Further analysis is required for comparing the PIV results to the 3D URANS CFD case seen in figure 3.12. While some consistencies are seen in the gradients and general height of the separated region, there is a contrast to the freestream velocity. The CFD model accurately predicts a shock near the crest just before the injection ports. This is identified in the Schlieren images as well, however the shock dissipates after several seconds once the separation bubble is abated. In the PIV vector fields a sharp gradient is observed in the freestream flow path. As the velocities measured downstream of the sharp gradient are significantly lower, this may imply the presence of a shock. Raw images also indicate a concentration of light which would result in an increased particle density at the shock.

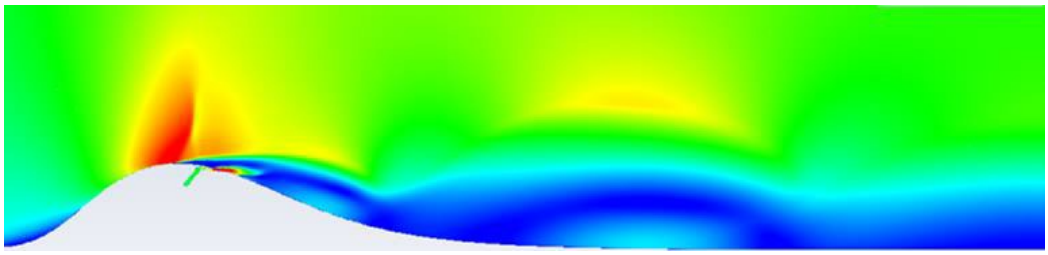

Figure 3.13 Instantaneous Mach Contours [5]

3.5 Uncertainty Analysis

The measurement system uncertainty discussed in section 2.4 explains that the source of the error comes from the ability to resolve the true distance travelled by the imaged particle in the given time. The magnification of the camera lens takes an important role as this determines the size of the imaged particle. The magnification also determines the DSR or the number of resulting vectors possible through the cross-correlation method. DaVis 8 provides an uncertainty quantification that employs a correlation statistics-based method [6]. This method is essentially the difference of the correlation maps between the two interrogation window sizes used. If the correlation maps have a symmetric correlation peak, the uncertainty in the resulting vector field is low. Note that with the size of the interrogation window, an average velocity is given to that area. In the case of resolving sharp gradients, a larger interrogation window will result in a broader gradient and become more refined during the subsequent passes at a smaller window size.

Figure 3.13 displays the velocity profiles in the spanwise direction for the two heat exchangers and the non-blowing instance of the wall-mounted hump. Due to the nature of the correlation peak of the blowing case, the uncertainties are considerably high.

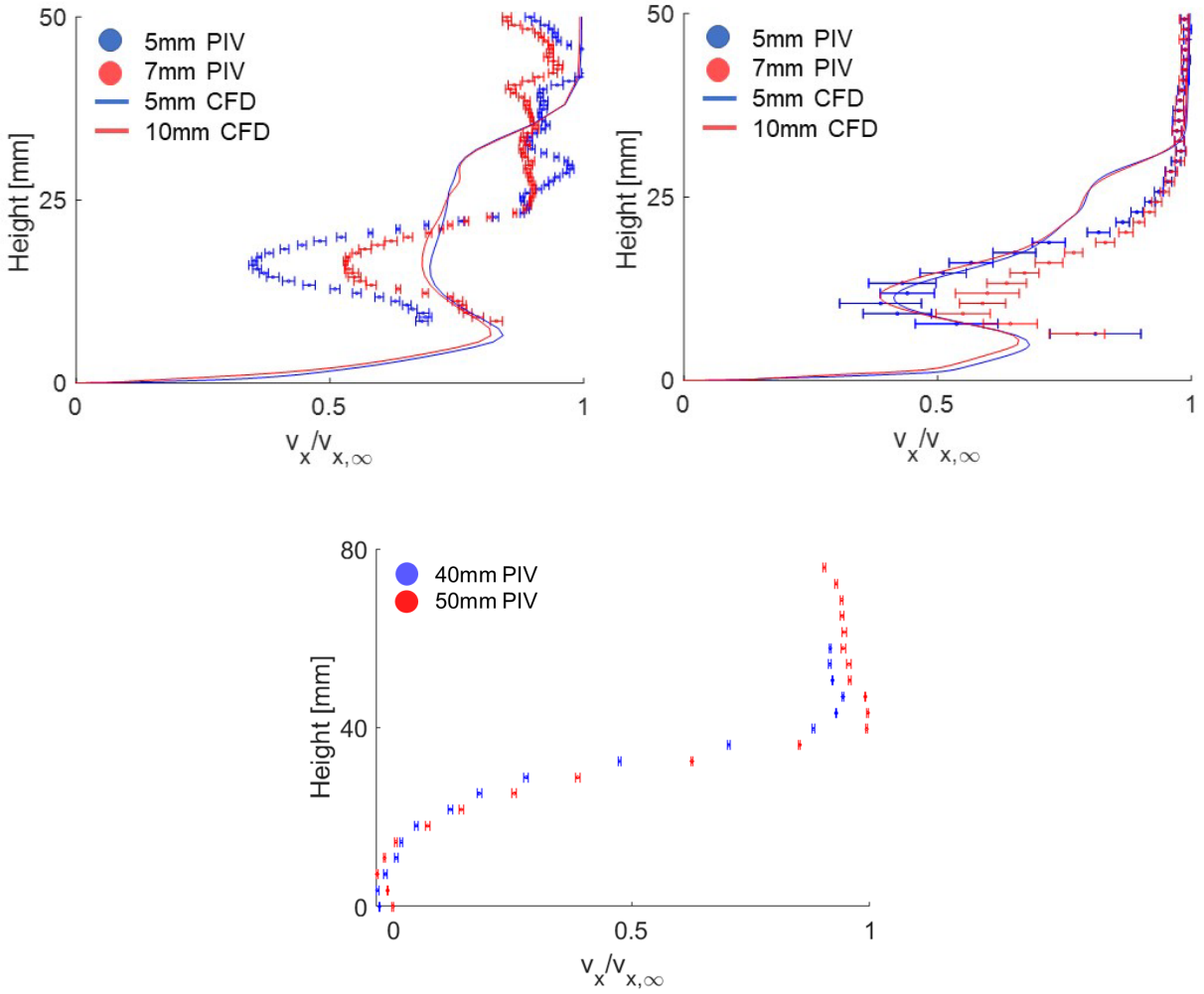

Figure 3.14 Velocity Profiles for Heat Exchangers and Non-Blowing Wall-Mounted Hump

The velocity plots above indicate how the uncertainty quantification works in DaVis 8. Note the scales for the uncertainties are scaled to the freestream velocities for each case. The magnitude of the uncertainties for the baseline and optimized heat exchangers are 1.3 and 3.5 whereas the non-blowing wall-mounted hump has a magnitude of 50. One noticeable attribute to these scales and the velocity plots are the number of data points. The baseline heat exchanger shows the smallest uncertainty and has the most vector points by almost twice that of the optimized geometry. Furthermore, the wall-mounted hump has 20 to 25 data points covering a span of 80mm. This is due to the spatial range attributed the camera settings. Based on the field of view and the magnification, the DSR significantly reduced. This is coupled with the relation between neighboring vectors. In the separated or freestream regions, the uncertainties reduce to

2m/s or less. Meanwhile, the larger uncertainties occur near sharper gradients as is the case in the wall-mounted hump. The baseline heat exchanger depicts how closer neighboring vectors can mitigate this large uncertainty as more vectors are resolved due to the higher DSR. Note that the baseline geometry's highest uncertainties occur around 40mm in height where the velocity reaches a sharp gradient as it increases towards $V_{x,\infty}$.

While the image particle velocity error measurement and the correlation statistics-based uncertainty quantification take different approaches to determining the error in the measurement system, both rely on the magnification of the camera and the resulting dynamic spatial range. It is essential to optimize these parameters to improve the spatial resolution.

4 CONCLUSIONS

The objective of this thesis is out to **develop an adaptable PIV measurement system for transonic internal flows**. Experimental results with a focus on characterizing separated regions is provided to assess the strategy taken to achieve this objective. The initial effort of the **development of an adaptable seeding technique** proved successful in understanding the fluid dynamics and the resulting response of the particles. The performance of an oil-based seed particle is determined based on the flow conditions and geometry of the experiment. The theoretical particle dynamics and measured outcome show positive results given a 10ms sampling time. Further work is required to improve the continuous seeding of the test section to allow for multiple measurements in long duration test.

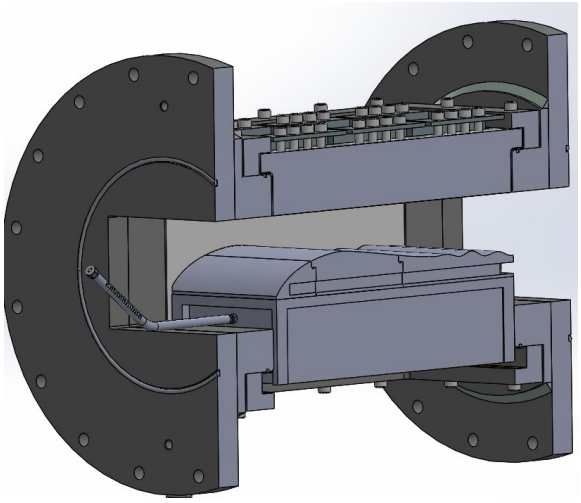

Figure 4.1 LEAF with Local Seeding Port with Rake Attached

Local seeding rakes are designed to ensure direct injection into the test section as primed particles in the settling chamber may accumulate and rest inside the chamber. An external accumulator tank is considered as the seed priming container with assistance from a second nitrogen line to assist in seed injection into the test section. This smaller tank ensures a denser seed injection. The inclusion of the external nitrogen line will assist in pressure differentials at the injection site when faced with higher flows. Further calibrations are required to determine the seed density and particle size in this configuration, as well as any flow perturbations caused by the rake upstream of the test section.

Optics optimization parameters are defined and given a detailed explanation of their significance in yielding a high dynamic velocity range and dynamic spatial range. The **optics optimization tool** proved beneficial and accurate when designing the ideal set up and the physical setup given the constraints around the test section. The excel tool is ready for future experiments, and is currently used in the setup for the future work in the adaptable seeding technique. Several test cases are discussed with comparisons to the theoretical optimizations and the final measurement system setup. While physical constraints impeded higher spatial resolution, modern cross-correlation software is employed to gain a sufficient spatial resolution to extract velocity fields from the measurements. The maximum and minimum velocities resolved are well within the bounds of the determined DVR given a transonic case. Future measurements in the PETAL facility at supersonic conditions will require more advanced techniques as discussed in the PIV review to resolve the full scale. Regarding the optical setup for the laser light sheet, a preprogrammed tool is constructed for future PIV measurements to determine the thickness and height of a light sheet design for given inputs of the lens array used. While not a novel concept, these quick calculations will aide in determining the physical setup required for the optical train.

Defining the above particle and optical settings to determine the expected **measurement system uncertainty** in the PIV setup proved useful in refinements throughout the development of the experiment prior to execution. While this uncertainty varies from the quantification determined by DaVis 8, both rely on the spatial resolution of the setup and the characteristics of the particle. Determining the image particle velocity measurement uncertainty and DSR will assist in understanding the expected uncertainty quantifications from the cross-correlation method.

After the implementation of the methodology, analysis on the flow fields is done to determine the strength of the results. The statistical tools available on commercial cross-correlation software allow the PIV user to assess accuracy, and what considerations must be taken in the future. Understanding the relation between the ideal interrogation window sizes for initial and subsequent passes to the spatial range will ensure immediate and accurate results. This plays a crucial role in resolving sharp gradients and turbulent structures typical near the separation bubble with a low uncertainty.

The experiments discussed in this work focused on the reduction of separation regions through geometrical optimization and active flow control strategies. Time-averaged vector fields and their associated velocity profiles are compared to CFD models with good matching in the finned heat exchangers and the non-blowing wall-mounted hump. Time-resolved PIV is shown for the non-blowing wall-mounted hump for the full sample of the measurement and is supported by another optical technique in its findings. The results for these experiments validate the methodology for this work, and the objective to create an adaptable PIV measurement system for transonic flows is achieved. Future experiments at the PETAL facility have a holistic tool to design, prepare, and execute PIV measurements.

REFERENCES

[1] Raffel, M., Willert, C.E., Scarano, F., Kähler, C.J., Wereley, S.T. and Kompenhans, J., "Particle image velocimetry: a practical guide," Springer, 2018. doi: 10.1007/978-3-540-72308-0.

[2] Ertürk Düzgün, N. (2012). *Particle image velocimetry applications in complex flow systems* (Doctoral dissertation, Universitat Rovira i Virgili).

[3] Molezzi, M. J., & Dutton, J. C. (1993). Application of particle image velocimetry in high-speed separated flows. *AIAA journal*, *31*(3), 438-446.

[4] Steven J Beresh 2021 *Meas. Sci. Technol.* 32 102003

[5] Steven Beresh *et al* 2015 *Meas. Sci. Technol.* 26 095305

[6] R J Adrian 1997 *Meas. Sci. Technol.* 8 1393

[7] Hain, R., Kähler, C.J. Fundamentals of multiframe particle image velocimetry (PIV). *Exp Fluids* 42, 575–587 (2007). https://doi.org/10.1007/s00348-007-0266-6

[8] Persoons, T., & O'Donovan, T. S. (2010). High dynamic velocity range particle image velocimetry using multiple pulse separation imaging. *Sensors*, *11*(1), 1-18.

[9] Chávez-Modena, M., González, L. M., and Valero, E., 2022, "Numerical Optimization of the Fin Shape Experiments of a Heat Conjugate Problem Surface Air/Oil Heat Exchanger (SACOC)," International Journal of Heat and Mass Transfer, 182, p. 121971.

[10] Nowak, H., Lluesma-Rodriguez, F., Rahbari, I., Clark, J., Paniagua, G., 2022, "Response of Separated Boundary Layers to Steady and Pulsated Flow Injection in Transonic Internal Flows," Turbomachinery Technical Conference & Exposition, GT2022-83152

[11] LaVision, 2018, "PIV Uncertainty Quantification," DaVis 8.4.0., June 2018, LaVision GmbH, Anna-VandenHoeck-Ring 19, D-37081.